

2016

Study of n-type metal oxide gas sensors utilizing Surface Acoustic Waves (SAW)

Master thesis

DIMITRA KATERINOPOLOU



Foundation for
Research
and Technology Hellas



University of Crete

University of Crete
Department of Physics

With the support of the
Foundation for Research and Technology
Institute of Electronic Structure & Laser

Master thesis

“Study of n- type metal oxide gas sensors utilizing
Surface Acoustic Waves (SAW)”

Dimitra Katerinopoulou

Supervising Committee

Prof. George Kiriakidis

Assist. Prof. Eleftherios Iliopoulos

Principal Researcher Stavros Pissadakis

Abstract

This study focuses on the investigation of ozone (O_3) gas sensing properties of metal oxides. The sensing material applied was zinc oxide (ZnO) and was selected for various reasons, such as natural availability, non-toxicity, high stability and piezoelectric properties. The deposition of the material was carried out via DC magnetron sputtering at different thicknesses. The structural and optical properties of ZnO were studied via X-Ray diffraction and spectrophotometry techniques respectively. These techniques revealed that the metal oxide fabricated had a preferred growth orientation along the c-axis, a high transparency exceeding 80% and an energy gap (E_g) of $\sim 3.31\text{eV}$. The sensing properties of ZnO were tested via two different techniques, of which the conductometric was used as a bench mark for the study of the material sensing responses through surface acoustic wave (SAW) utilizing commercial transducers at very high frequency ($\sim 1\text{GHz}$). A set of different O_3 concentrations levels ranging from 6ppb to 2ppm for the conductometric and from 110ppb to 2ppm for the SAW tests were applied. The motivation behind the use of acoustic sensors was their small size, inexpensiveness, sensitivity and their response to a large range of oxidizing and reducing gases. The investigation has shown that there is an operating limit for the said commercial transducers which restricted the sensing operation thicknesses on the SAW to below 100nm. The testing gas selected was ozone due to its critical importance in our environment and its impact on human health. Ozone becomes harmful for human health for concentrations above 50ppb according to EPA and WHO. The conductometric tests lead to the result that most of the samples exhibit an up to 5 orders of magnitude response and for thicknesses above 100nm the sensor (on glass substrates) can distinguish among different ozone concentrations with relatively adequate accuracy. Similarly, results obtained through the SAW technique did show a good response also, with a maximum frequency shift value of 8-9MHz, during their first photoreduction- oxidation cycle. Detailed study of the SAW sensing responses demonstrated, for the first time, the role of sensing substrates on their response rate and form. This study revealed the complexity of acoustoelectric and mechanical properties for the SAW transducers in the process of

accurate and reproducible sensing results. Nevertheless both techniques were found to have a good reversibility during their photoreduction–oxidation processes which merits them as durable sensing devices for room temperature applications.

Περίληψη

Η παρούσα μεταπτυχιακή εργασία εστιάζει στη μελέτη των ιδιοτήτων των οξειδίων των μετάλλων ως αισθητήρες ανίχνευσης όζοντος. Το υλικό που χρησιμοποιήθηκε ήταν το οξείδιο του ψευδαργύρου για διάφορους λόγους, όπως ότι υπάρχει άφθονο στη φύση, είναι μη τοξικό, παρουσιάζει υψηλή σταθερότητα και έχει πιεζοηλεκτρικές ιδιότητες. Η εναπόθεση του υλικού έγινε με DC magnetron sputtering για διαφορετικά πάχη. Οι δομικές και οπτικές ιδιότητες του οξειδίου του ψευδαργύρου μελετήθηκαν με την τεχνική περίθλασης ακτίνων-X και φασματοφωτομετρία αντίστοιχα. Από αυτές εξάγαμε ότι το υλικό μας είχε προτιμητέα διεύθυνση ανάπτυξης κάθετα στο υπόστρωμα, παρουσίασε υψηλή διαπερατότητα μεγαλύτερη από 80% και το ενεργειακό χάσμα υπολογίστηκε να είναι περίπου 3.31eV. Οι ιδιότητες ως προς την ευαισθησία μελετήθηκαν μέσω δύο διαφορετικών τεχνικών, η μία ήταν η μέτρηση ως προς την αλλαγή των ηλεκτρικών χαρακτηριστικών και η άλλη αυτή των επιφανειακών ακουστικών κυμάτων (SAW) στην οποία χρησιμοποιήθηκαν εμπορικά φίλτρα υψηλής συχνότητας (~1GHz). Πραγματοποιήθηκε μια σειρά πειραμάτων με διαφορετικές συγκεντρώσεις όζοντος, οι οποίες κυμάνονταν από 6ppb έως 2ppm για τις μετρήσεις ως προς την αλλαγή της αγωγιμότητας και από 100ppb έως 2ppm για την τεχνική των SAW. Το κίνητρο για τη χρήση των ακουστικών αισθητήρων ήταν ότι έχουν μικρό μέγεθος, είναι οικονομικοί και παρουσιάζουν ευαισθησία και καλή απόκριση σε ένα μεγάλο εύρως οξειδωτικών και αναγωγικών αερίων. Από τη μελέτη μας, εξάγαμε ότι υπάρχουν κάποια όρια αντοχής για τα φίλτρα που χρησιμοποιήθηκαν τα οποία περιορίζουν τα όρια ανίχνευσης για πάχη κάτω από 100nm. Το προς ανίχνευση αέριο επιλέξαμε να είναι το όζον για το λόγο ότι βρίσκεται σε μεγάλες ποσότητες στο περιβάλλον και επηρεάζει την υγεία του ανθρώπου. Συγκεκριμένα το όζον είναι ιδιαίτερα επιβλαβές για τον άνθρωπο για συγκεντρώσεις μεγαλύτερες από 50ppb σύμφωνα με τον Οργανισμό Προστασίας του Περιβάλλοντος. Τα πειράματα ως προς την αλλαγή της αγωγιμότητας έδειξαν ότι τα περισσότερα δείγματα δίνουν απόκριση έως και 5 τάξεις μεγέθους, και για πάχη πάνω από 100nm ο αισθητήρας μπορεί να διαχωρίσει

με ακρίβεια τις διαφορετικές συγκεντρώσεις όζοντος που εισάγαμε στο θάλαμο. Ομοίως, τα αποτελέσματα που εξάγαμε από την τεχνική των επιφανειακών ακουστικών κυμάτων έδειξαν επίσης πολύ καλή απόκριση με τη μέγιστη μεταβολή της συχνότητας να είναι 8-9MHz, κατά τη διάρκεια του πρώτου κύκλου φωτοαναγωγής – οξείδωσης. Λεπτομερής μελέτη των αποκρίσεων με την τεχνική των SAW, έδειξε για πρώτη φορά, την επίδραση του υποστρώματος στο ρυθμό και τη μορφή της απόκρισης. Αυτή η μελέτη απέδειξε την πολυπλοκότητα των ακουστοηλεκτρικών και μηχανικών ιδιοτήτων των μετατροπέων κατά τη διαδικασία ανίχνευσης με αποτελέσματα ακρίβειας και αναπαραγώγημα. Παρ' όλα αυτά, και οι δύο τεχνικές βρέθηκε να έχουν καλή αναστρεψιμότητα κατά τη διαδικασία της φωτοαναγωγής – οξείδωσης το οποίο τις ορίζει ως ανθεκτικές διατάξεις ανίχνευσης για εφαρμογές σε θερμοκρασία δωματίου.

Acknowledgements

First of all I would like to thank my thesis advisor Prof. George Kiriakidis from the Physics Department of University of Crete. I am grateful of having the chance to benefit from his knowledge and expertise. He consistently allowed this thesis to be my own work, but steered me in the right direction whenever he thought it was necessary.

I would also like to thank the experts who were involved in the validation survey for this thesis: Assistant Professor, Eleftherios Iliopoulos from the Department of Physics of the University of Crete and Principal Researcher, Stavros Pissadakis from Foundation for Research & Technology- Hellas at the Institute of Electronic Structure and Laser for their support and comments.

Furthermore, I would like to thank Dr. Konstantinos Moschovis and Mr. Emmanouil Gagaoudakis for providing me with training aspects as well as knowledge and expertise. This thesis would not have been completed without their significant contribution. It would be a great miss if I would have not recognized the continuous support of all the TCM group members.

Finally, I must express my very profound gratitude to my parents, Asimina and Elias and to my sister Alexandra, for providing me with unfailing support and continuous encouragement throughout the period of my studies. This accomplishment would not have been possible without them. Thank you.

Dimitra Katerinopoulou

Heraklion,

June, 2016

Contents

| | |
|---------------------------------------|----|
| Abstract | 2 |
| Περίληψη | 4 |
| Acknowledgements | 6 |
| List of abbreviations | 8 |
| List of Figures | 9 |
| List of Tables | 10 |
| Introduction | 11 |
| Chapter 1 | 12 |
| Basic background notes | 12 |
| 1.1 Zinc oxide characteristics | 12 |
| 1.2 Ozone characteristics | 14 |
| 1.3 Sensors | 15 |
| 1.4 Piezoelectricity | 18 |
| 1.5 Surface acoustic waves..... | 19 |
| Chapter 2 | 27 |
| Experimental | 27 |
| 2.1 Deposition technique | 27 |
| 2.2 Characterization technique | 29 |
| 2.2.1 Structural properties | 29 |
| 2.2.2 Optical properties..... | 32 |
| 2.3 Sensing techniques..... | 34 |
| 2.3.1 Conductometric..... | 34 |
| 2.3.2 Surface acoustic waves..... | 36 |
| Chapter 3 | 38 |
| Results | 38 |
| 3.1 Characterization Techniques | 38 |
| 3.2 Sensing..... | 42 |
| Conclusions | 59 |
| References | 62 |
| Appendix I | 67 |
| Appendix II | 70 |

List of abbreviations

| | |
|----------------|---|
| ZnO | Zinc oxide |
| O ₃ | Ozone |
| O ₂ | Oxygen |
| N ₂ | Nitrogen |
| SAW | Surface Acoustic Waves |
| ppb | parts per billion |
| ppm | parts per million |
| sccm | standard cubic centimeters/min |
| IDT | Interdigital Transducers |
| UHV | Ultra-High Vacuum |
| XRD | X-Ray Diffraction |
| SEM | Scanning Electron Microscopy |
| UV/VIS/NIR | Ultra Violet/Visible/Near Infrared |
| JCPDS | Joint Committee on Powder Diffraction Standards |
| EPA | Environmental Protection Agency |
| CVD | Chemical Vapor Deposition |
| PVD | Physical Vapor Deposition |

List of Figures

- Figure 1* Schematic representation of ZnO crystal structures of a wurtzite and a zinc blende
- Figure 2* Schematic diagram of a sensor
- Figure 3* Relation among mechanical and electrical variables for a crystal
- Figure 4* Illustration of the particle displacements during propagation of (a) z-polarized, z-propagating compressional wave (b) y-polarized, z-propagating shear wave and (c) the combination that forms the surface acoustic wave
- Figure 5* Typical SAW device
- Figure 6* Fractional change in SAW propagation velocity and attenuation vs thickness of an evaporated metal film.
- Figure 7* Acoustoelectric velocity and attenuation vs sheet conductivity
- Figure 8* DC sputtering set up
- Figure 9* Geometry of the sample
- Figure 10* Constructive & distractive interference wave
- Figure 11* X-ray diffraction (Bragg's Law)
- Figure 12* A simple UV/Visible spectrophotometer
- Figure 13* Schematic of conductivity-based system for photo-reduction and oxidation processes
- Figure 14* Home-made cell hosting SAW filter
- Figure 15* XRD pattern of ZnO thin film deposited at different deposition rates
- Figure 16* Cross-sectional SEM image of ZnO thin film a) 230 nm & b) 105 nm
- Figure 17* Transmittance spectra of ZnO thin films
- Figure 18* Energy gap & grain size as function of thickness
- Figure 19* a) Photoreduction-oxidation process of ZnO film 230nm,
b) Normalized exponential decay curves of 230nm
- Figure 20* a) Photoreduction-Oxidation process of ZnO film 205nm,
b) Normalized exponential decay curves of 205nm
- Figure 21* a) Photoreduction-Oxidation process of ZnO film 105nm,
b) Normalized exponential decay curves of 105nm
- Figure 22* a) Photoreduction-Oxidation process of ZnO film 63nm,
b) Normalized exponential decay curves of 63nm

| | |
|------------------|---|
| <i>Figure 23</i> | a) Photoreduction-Oxidation process of ZnO film 30nm, b) Normalized exponential decay curves of 30nm |
| <i>Figure 24</i> | Sensitivity as a function of concentration for all thicknesses |
| <i>Figure 25</i> | Repeatability of ZnO 205nm thickness |
| <i>Figure 26</i> | Stability of ZnO 205nm after 3 months |
| <i>Figure 27</i> | a) Frequency shift, b) Phase shift due to ZnO deposition |
| <i>Figure 28</i> | Frequency shift due to sensing layer deposition, a): 30nm, b): 63nm & c): 105nm |
| <i>Figure 29</i> | Operating frequency dependence vs ZnO deposition duration |
| <i>Figure 30</i> | 930MHz SAW filter response toward different O ₃ concentrations at RT a) 105nm, b) 63nm, c) 30nm |
| <i>Figure 31</i> | Detailed representation of photoreduction-oxidation procedure through SAW device |
| <i>Figure 32</i> | Repeatability of filter 930 MHz with 30nm thickness |

List of Tables

| | |
|----------------|-------------------------------------|
| <i>Table 1</i> | Ozone ppb levels and air quality |
| <i>Table 2</i> | Structural results |
| <i>Table 3</i> | Recorded frequency & insertion loss |

Introduction

Sensing of hazardous gases has been of great importance during the last decades. For this purpose many materials, mainly metal oxides, have been studied and tested in as far as their sensing characteristics are concerned. Zinc oxide is a well-known wide band gap semiconductor which is used in many applications due to its excellent optical, structural and electrical properties. In addition, its surface chemical sensitivity along with the variation of conductivity when reacting with oxidizing gases, such as ozone, makes it an appropriate candidate as gas sensing material (Bender et al., 2003). The sensing mechanism is based on the absorption of ozone molecules on its surface, which induces changes in the film conductivity (Atashbar et al., 1999). Accurate recording of these conductivity changes lead to the well-established conductometric sensing technique utilized by a number of commercial sensors such as the Taguchi (Taguchi, 1972). However, making use of these transport properties of films deposited on suitable piezoelectric substrates, one may utilize the induced variations in the propagation of the surface acoustic wave (SAW) in order to detect absorbed oxidizing or reducing gases.

The scope of this work was to investigate the operational limitations of commercial high frequency SAW transducers coated with ZnO as active material for ozone detection. In this context, a literature background on Zinc oxide, as ozone sensing element along with acoustic wave based sensors with a brief reference to piezoelectricity are presented in chapter 1. Chapter 2, describes in detail the experimental procedure followed regarding the deposition, as well all the characterization techniques (both structural and optical) used. The chapter concludes with an evaluation of the sensing mechanisms involved. Finally, the work concludes with Chapter 3, in which all results are presented along with an overall discussion and comparison with the open literature reports.

Chapter 1

Basic background notes

1.1 Zinc oxide characteristics

Zinc oxide is an inorganic compound with the formula ZnO. It is a white powder that is insoluble in water. It belongs in II – IV category of semiconductors with a wide direct bandgap of 3.37 eV at room temperature (RT) and 3.44 eV at 4 K (Li et al., 2004), (Bender et al., 2003). Advantages associated with a wide band gap include higher breakdown voltages, ability to sustain large electric fields, lower electronic noise, and high-temperature and high-power operation. ZnO is an n-type semiconductor (Look, 2001), (Suchea et al., 2006), (Christoulakis et al., 2006), (Kortidis et al., 2009) due to oxygen vacancies or zinc interstitials and crystallizes in two main structures, wurtzite of hexagonal phase and zinc blende of cubic phase

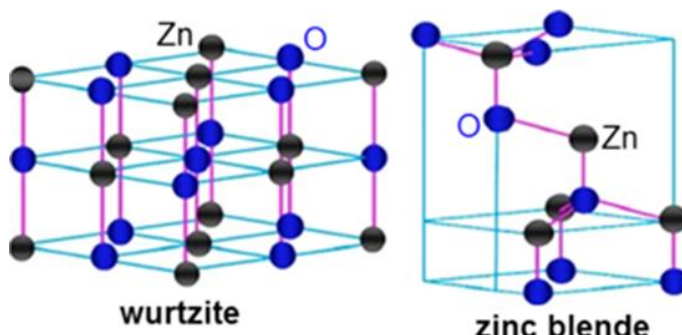


Figure 1: Schematic representation of ZnO crystal structures of a wurtzite and a zinc blende. Source (Ashrafi et al., 2013)

with tetrahedral coordination geometry in both cases.(Lee, et al., 2002)(Martinez-Perez et al., 2015)(Ü Özgür et al., 2005). The lattice constants are $a = 3.25 \text{ \AA}$ and $c = 5.2 \text{ \AA}$, their ratio $c/a \sim 1.60$ is close to the ideal value for hexagonal

cell $c/a = 1.633$. However at ambient conditions (temperature and pressure) ZnO crystallizes normally in a wurtzite structure having a lattice with two interconnecting sub-lattices of Zn^{2+} and O^{2-} with the zinc ion be surrounded by tetrahedral oxygen ions and vice versa. This tetrahedral coordination give rise to a polar symmetry along the hexagonal axis, which is responsible for a number of physical and chemical properties, including piezoelectricity and spontaneous polarization. The structure of

ZnO is a key factor in crystal growth, etching and defect generation (Arya et al., 2012). Point defects on ZnO surfaces are extremely important in gas sensing as they produce very large changes in the surface conductivity. The changes occur at the surface of the grains as a result of charge transfer and band bending caused by the adsorbates. The dominant defects are O vacancies. These defects do not produce any new electronic states in the bandgap. This is related to the range of stable oxidation states (Eranna et al., 2016).

Nanostructures of ZnO can be synthesized into a variety of morphologies including nanowires, nanorods, tetrapods, nanobelts, nanoflowers, nanoparticles etc. Nanostructures can be obtain by various techniques, at certain conditions, such as hydrothermal synthesis or melt growth, chemical vapor deposition (Ma et al., 1996), metalorganic vapour phase epitaxy, electrodeposition, pulsed laser deposition, sputtering (Li et al., 2004), sol-gel synthesis, atomic layer deposition, spray pyrolysis (Kortidis et al., 2009) and others (Jin et al., 1994), (Bender et al., 2003). Especially, nanowires have attached a lot of attention due to their good charge carrier transport properties and high crystalline quality (Özgür et al., 2010)

Over the last two decades, intense research is focused on zinc oxide, among other, due to its natural availability, its non-toxicity, and the wide range of its electrical resistivity which can extend from 10^{-4} to 10^{12} Ωcm according to the deposition conditions and simplicity in fabrication (Bedia et al., 2014). Zinc oxide is also one of the most preferable metal oxide material (together with In and Sn) for gas sensing applications due to its high sensitivity (M. Bender et al., 2002), high resistivity and perfect c – axis orientation texture which shows piezoelectric effect. Due to its high stability, melting point and excitation binding energy (60meV), (Shokry Hassan et al., 2014),(Tseng et al., 2015),(Ü Özgür et al., 2005) ZnO is potentially a very promising optoelectronic material (Li et al., 2004). The large piezoelectric coefficient of ZnO, specifically along the c-direction has allowed for the development of surface acoustic wave (SAW) devices that can operate particularly at higher frequencies than other devices (Arya et al., 2012). Thus, a significant part of the recent research in the field of ZnO-based devices and applications deals with ZnO nanostructures and their integration with the mainstream semiconductor materials (Ümit Özgür et al., 2010).

1.2 Ozone characteristics

Ozone is an inorganic molecule with the chemical formula O₃. It is colorless or slightly bluish blue gas (when liquefied). Ozone is an important component of smog, is a highly reactive and unstable gas capable of damaging living cells. As pollutant it is formed in the atmosphere through complex reactions between chemicals directly emitted from vehicles, industrial plants, and many other sources (“Ozone and Health,” 2015). It is a strong oxidizing pollutant that is often present in the ground level environment at concentrations known to have harmful health and ecological effects (Bagad, 2009). The highest levels of ozone in the atmosphere, are in a region also known as the ozone layer between about 10 km and 50 km above the surface. However, even in this “layer”, the ozone concentrations are only two to eight parts per million (ppm), so most of the oxygen there remains of the dioxygen type.

According to the U. S. Environmental Protection Agency (EPA), ozone concentrations of more than 75 parts per billion (ppb) are very dangerous for human health. EPA announced that levels close to 100 ppb may irritate breathing diodes and eyes. In the following Table 1 are presented different ppb levels based on 8 hour average concentrations as a function of the air quality and given cautionary statements for O₃.

Table 1: Ozone ppb levels and air quality Source: EPA

| Air Quality Index for Ozone <small>(based on 8-hr average concentrations)</small> | | |
|--|-----------------------------------|---|
| Index Values (Conc. Range) | Air Quality Descriptors | Cautionary Statements for Ozone |
| 0 – 50 (0-59 ppb) | Good | No health impacts are expected when air quality is in this range. |
| 51 – 100 (60-75 ppb) | Moderate | Unusually sensitive people should consider limiting prolonged outdoor exertion |
| 101 – 150 (76-95 ppb) | Unhealthy for Sensitive Groups | Active children and adults, and people with respiratory disease, such as asthma, should limit prolonged outdoor exertion |
| 151 – 200 (96-115 ppb) | Unhealthy | Active children and adults, and people with respiratory disease, such as asthma, should avoid prolonged outdoor exertion; everyone else, especially children should limit prolonged outdoor exertion. |
| 201 – 300 (116-374 ppb) | Very Unhealthy | Active children and adults, and people with respiratory disease, such as asthma, should avoid all outdoor exertion; everyone else, especially children, should limit outdoor exertion. |

1.3 Sensors

Sensors are used in almost every field these days, ranging from very basic home appliances, advanced medical devices, automotive industry to space vehicles. Investigation of new types of sensors is required to address the needs of the developing technology. Hence sensors have become an emerging technology and currently have been investigated in wide-variety of technological areas(Manohar, 2012).

A sensor is a device that responds to a physical, chemical, biological, or electric stimulus by producing, usually an output signal that is a function of the input stimulus, as indicated in figure 2.

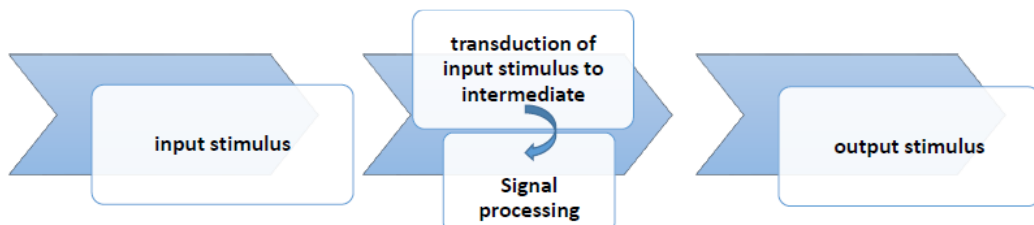


Figure 2: Schematic diagram of a sensor

Inside a typical sensor, a process of transduction takes place, converting the input event into usually an electrical signal. The output signal may be stored in a computer memory for later examination. Possible applications would have the signal activating an alarm to warn of the presence of a toxic vapor, or combining with other signals to provide for instance a physician with information on which to base a medical decision.

Gas sensors

Gas sensors have been extensively used to detect and monitor a wide variety of radical gases. In particular, gas sensors have a huge variety of applications such as in environmental quality control, public safety, medical applications, automotive applications and for air conditioning systems in aircrafts, space crafts, vehicles and

houses (Kiriakidis et al., 2012). Gas detection using semiconducting materials has had considerable impact to date. However, the need to operate at high temperatures often limits the use of this type of detection. For these reasons, proposals have been made to modify some of the structural parameters (crystal shape and orientation). Nanostructured materials can be used to reduce the temperatures and they consume less power and so are safer to operate.

Nanostructured metal oxides are one of the main types of materials used to fabricate gas sensors. The semiconducting nature of these compounds may induce the electrical conductivity of the material to change when the composition of the surrounding atmosphere changes. This means that most of these devices can be classified as conductometric nanosensors (Jiménez-Cadena et al., 2007).

As in all types of sensors, gas sensors have certain parameters too which characterized them. The most important parameters and their definitions are described below.

Sensitivity

The sensitivity of a sensor is defined as the ratio of the change amplitude of a sensor signal to the original amplitude which is defined as:

$$S = \frac{\Delta R}{R} \times 100\% \quad (1)$$

Where ΔR is the change amplitude of the sensor signal, and R is the amplitude of the original signal. The signal could be the resistance, current, voltage or conductance, etc. (Wei et al., 2011). This parameter is sometimes confused with the detection limit.

Selectivity

The selectivity of a sensor is a measure of its response to a certain object compared to other (Wei et al., 2011), and for a gas sensor defines its ability to distinguish signals from similar oxidizing or reducing gases.

Stability

Stability is the ability of a sensor to provide reproducible results for certain period of time. This includes retaining its sensitivity, selectivity, response and recovery time.

The stability of a sensor is evaluated by the change of sensing behavior after numerous times of switching between ‘ON’ state and ‘OFF’ state (Wei et al., 2011).

Repeatability

Repeatability is the ability of a sensor, to give the same response for consecutive cycles under identical conditions.

Detection limits

Detection limits is the lowest concentration that can be detected by the sensor under given conditions, particularly at a given temperature (Bochenkov et al., 2010).

Response time

Is the time required by a sensor to respond to a step concentration change from zero to a certain concentration value (Bochenkov et al., 2010).

Recovery time

Is the time it takes for the sensor signal to return to its initial value after a step concentration (Bochenkov et al., 2010).

Acoustic wave based sensors

Acoustic wave devices are based on frequency mechanical vibrations. Acoustic-wave based sensors offer a simple, direct and sensitive method for probing the chemical and physical properties of materials. A basic advantage is that acoustic waves travel very slowly (typically 3000m/s), so that large delay lines are obtainable. The term acoustic is commonly used in literature, even when referring to frequencies which are well above the audible range (Comini et al., 2009). Acoustic waves cover a frequency range of 14 orders of magnitude- from 10^{-2} Hz (seismic waves) and extending to 10^{12} Hz (thermos-elastic excited phonons) (Janshoff et al.,2000).

1.4 Piezoelectricity

Electronic devices, generate SAWs from an electrical input signal and then use the SAWs to generate an electrical output signal. The conversion process is called “transduction.” To obtain this, we have to consider piezoelectricity, which is a property of many solid materials. The coupling between strain and electrical polarization that occurs in many crystals provides the means for generating acoustic waves electrically. When a structure of a crystal lacks a centre of inversion symmetry, the application of strain changes the distribution of charge on the atoms and bonds comprising the crystal in such a manner that a net, macroscopic, electrical polarization of the crystal results. Crystals exhibiting this direct piezoelectric effect always exhibit the converse effect as well, whereby the crystal is strained by the application of an electric field.

The piezoelectric effect occurs only in anisotropic materials, so that the properties depend on the orientation relative to the internal arrangement of atoms. Usually this means that crystalline materials must be used. Because of this, it is important to consider the cut and orientation of a piezoelectric material during the design and manufacture of a device. An important characteristic of these materials for use in SAW sensors is the mechanical strain ε . The mechanical strain ε which results from the application of a stress σ is linearly proportional to the compliance S ($S^{-1} = E_y$ = Young's modulus) within the elastic deformation region of the stress-strain curve of the material:

$$\varepsilon = S\sigma \quad (2)$$

Strain is a dimensionless property which describes the changes in length of a material, defined as the length under stress divided by the equilibrium (no stress) length of the material (Kirschner, 2010).

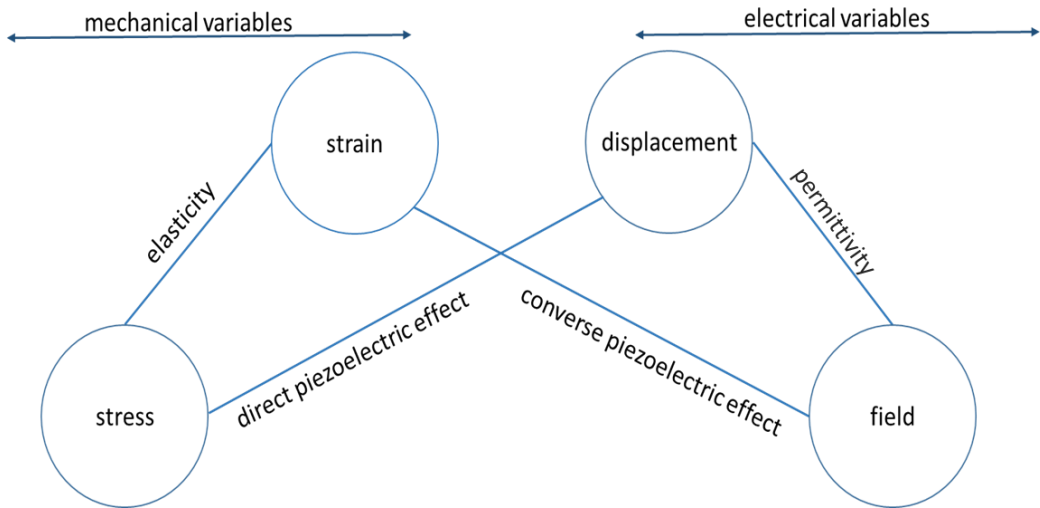


Figure 3: Relation among mechanical and electrical variables for a crystal

1.5 Surface acoustic waves

A surface acoustic wave (SAW) is a type of mechanical wave motion which travels along the surface of a solid material. The wave was discovered in 1885 by Lord Rayleigh, and is often named after him (Jakubik, 2011)(Hatch, 2000). Rayleigh showed that SAWs could explain one component of the seismic signal due to an earthquake and other vibrations that occurs on the surface of the Earth (Kirschner, 2010). Namely that at this mode of propagation the acoustic energy is confined very near the surface of an isotropic solid and decay into the depth within a distance of the order of a wavelength. It means that the wave is not uniform along the direction normal to the surface and hence it cannot be classified as a plane wave. Nowadays, these acoustic waves are often used in electronic devices.

A SAW is made up of a compressional wave and a shear wave coupled together in a fixed ratio with a phase difference. An illustration of the displacement that occur during propagation of a Rayleigh wave is shown in figure 4. The shear wave component creates a particle motion perpendicular to the direction of propagation while this motion is parallel for the compressional wave. When these two couple they form a surface acoustic wave and it can be seen that there are alternating

regions of tension and compression. Around region 1 the lines of the grid become closer to each other which indicates it is under compression whereas around region 2, which is under tension, the lines of the grid tend to diverge (Garza, 2013)(Comini et al., 2009).

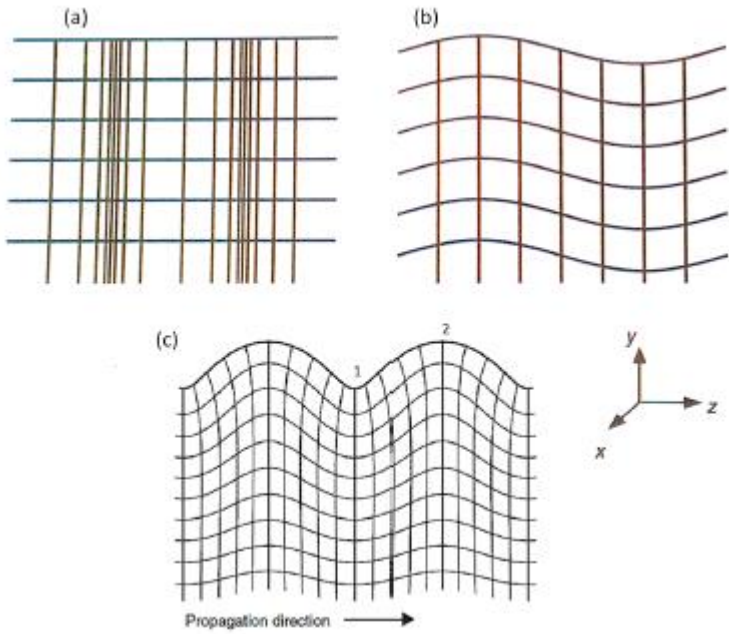


Figure 4: Illustration of the particle displacements during propagation of (a) z-polarized, z-propagating compressional wave (b) y-polarized, z-propagating shear wave and (c) the combination that forms the surface acoustic wave. Source: (Morgan, 2007)

Surface acoustic waves are modes of elastic energy propagation governed by the elastic wave equation and boundary conditions that specify a stress free surface. In three dimensions, there are three wave equations and three boundary conditions, which can both be formulated into matrix form.

Application of force to a solid puts a solid under stress. Stress results in strain within the solid: atoms or molecules of which the solid is composed are displaced from their unstressed locations. Definition of stress and strain permits derivation of the equation of motion for elastic deformations of a solid, in particular wave motion.

In the absence of external forces, the wave equation for an elastic homogeneous, anisotropic medium can be written as:

$$\rho \frac{\partial^2 u_i}{\partial t^2} = \sum_j^3 \frac{\partial T_{ij}}{\partial t^2} \quad (3)$$

where, u_i are the displacements measured along the x, y, z Cartesian axes. The density of the medium is ρ , and the stress tensor T_{ij} , neglecting piezoelectric effect is defined:

$$T_{ij} = \sum_{k,l=1}^3 C_{ijkl} S_{kl} \quad (4)$$

in which the C_{ijkl} , called elastic stiffness constants and S is the strain matrix. This equation called elastic constitutive relation.

From the elastic equation of motion and the elastic constitutive equation, it is a simple matter to derive the wave equation, which describes the propagation of plane acoustic waves in a non-piezoelectric solid.

$$\rho \frac{\partial^2 u_i}{\partial t^2} = \sum_{j,k,l=1}^3 C_{ijkl} \frac{\partial^2 u_k}{\partial x_j \partial x_l} \quad (5)$$

It should be noted that this equation represents a set of three wave equations ($i=1, 2, 3$) in the particle displacements u_1, u_2, u_3 , with summations over the indices j, k and l . The polarization of the wave refers to the direction of particle displacement.

SAW devices

The utility of Rayleigh waves in sensors application, as mentioned before, is also due to the surface confinement of energy, allowing them to be excited by surface electrodes in piezoelectric materials and also making the wave extremely sensitive to the surface perturbations.

A typical SAW device consists of two interdigital transducers (IDTs) on a piezoelectric substrate, usually single crystal of quartz, lithium niobate (LiNbO_3), lithium tantalate (LiTaO_3) or gallium arsenide (GaAs).

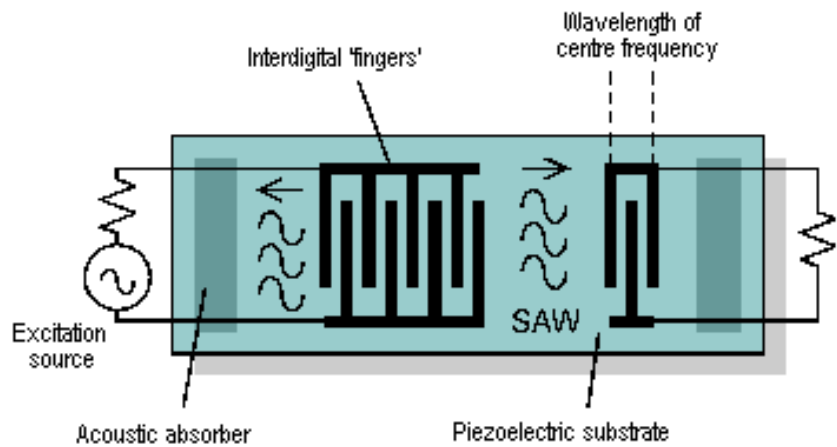


Figure 5: Typical SAW device

Saw excitation and detection

The discovery by R. M. White that surface acoustic waves could be excited and detected by lithographically patterned interdigital electrodes on the surface of piezoelectric crystals has led to widespread use of SAW devices in a number of signal-processing applications.

A surface acoustic wave is most conveniently excited on a piezoelectric crystal using an interdigitated transducer (IDT). Application of a voltage between alternately connected electrodes causes a periodic electric field to be imposed on the crystal. When an alternating voltage is applied, a periodic strain field is generated in the piezoelectric crystal that produces a standing SAW. This standing wave gives rise to propagating waves that are launched in both directions away from the transducer; the wavefronts are parallel to the transducer fingers.

The transducer operates most efficiently when the SAW wavelength, λ , matches the transducer periodicity, d . This occurs when the transducer is excited at the synchronous frequency, defined by $f_0 = v_0/d$, where v_0 is the SAW propagation velocity. The critical structures are arrays of narrow parallel metal fingers. In the IDT, parallel electrodes are connected alternately bus bars. The space between the fingers is $\lambda/2$ and the finger width is typically half of this, $\lambda/4$ (Comini et al., 2009).

Each transducer finger may be considered to be a discrete source for the generation of surface waves in a piezoelectric medium because the piezoelectrically generated stress varies with position near each transducer finger. A simple transfer function relates the continuous wave (CW) voltage V_i applied to a finger and the electrical potential associated with the waves radiated in each direction:

$$\varphi^\pm = \mu_s V_i \quad (6)$$

Where μ_s a substrate dependent constant, ϕ^+ is associated with the rightward propagating SAW, while ϕ^- is a leftward propagating SAW. The parameter μ_s may be considered frequency independent: the frequency response of the transducer arises mainly from interference between finger contributions, and is relatively insensitive to the frequency response of the individual elements (Ballantine et al., 1997).

Main interactions

When SAW devices are used for sensors, the measured responses arise from perturbations in wave propagation characteristics, specifically wave velocity and attenuation, resulting from interactions between the SAW and a surface layer. SAW film interactions that arise from mechanical coupling between the wave and film include mass loading caused by the translation of surface mass by the SAW surface displacement and elastic effects caused by SAW induced deformation of a surface film. SAW-film interactions that arise from electrical coupling between the wave and film include acoustoelectric interactions between electric fields generated by the SAW and charge carriers in a conductive film (Ballantine et al., 1997). It is important to note, that a sensor response may be due to a combination of these interactions, hence the problem of overlapping sensitivity need to be addressed (Hoummady et al., 1999). For this reason at this study, the mass loading effect for the operational limits of the SAW device were tested, and after that the Saw filters were used for the gas detection via the acoustoelectric effect interaction.

Mass loading

The simplest interaction, and the most utilized for SAW sensor applications, is the response due to changes in the areal/mass density on the device surface. The mass sensitivity of the different acoustic devices are related to the structure geometry and resonant centre frequency. In general the mass sensitivity for SAW devices increases with increasing the centre frequency (Hoummady et al., 1999). The effect on wave velocity and attenuation of this interaction may be derived from energy consideration.

Movement by the wave on the surface layer caused an increased in kinetic energy density, U_k of the wave without dissipating any wave energy. This is expected to change the wave velocity without affecting attenuation. An expression for the change in wave velocity arising from surface mass loading is:

$$\frac{\Delta v}{v_0} = - \left(\frac{v_{x0}^2}{\omega P} + \frac{v_{y0}^2}{\omega P} + \frac{v_{z0}^2}{\omega P} \right) \quad (7)$$

where v_{x0} , v_{y0} , and v_{z0} are the velocities, P is the power density and ω is the angular velocity. Obviously, the quantities in the parenthesis being independent of wave amplitude and depending only on the surface material, remain constant. Grouping all the substrate-dependent constants together results in an expression for mass-induced change in SAW propagation velocity:

$$\frac{\Delta v}{v_0} = -c_m f_0 \rho_s \quad (8)$$

where c_m is the mass sensitivity factor, ρ_s is the surface mass density and f_0 is the resonant frequency (Ballantine et al., 1997). The negative component causing a decrease of velocity (Jakubik, 2011).

An example of velocity and attenuation changes resulting from depositing a mass layer on a 97MHz SAW device using an ST-cut quartz substrate are shown in figure 6. (Ballantine et al., 1997). As it can easily be observed velocity decreases linearly with thickness whilst the relative attenuation change $\Delta\alpha/k$ (where α is the attenuation and $k = 2\pi/\lambda$ is the wavenumber) due to mass loading is negligible in comparison with $\Delta v/v_0$ shown on the same scale.

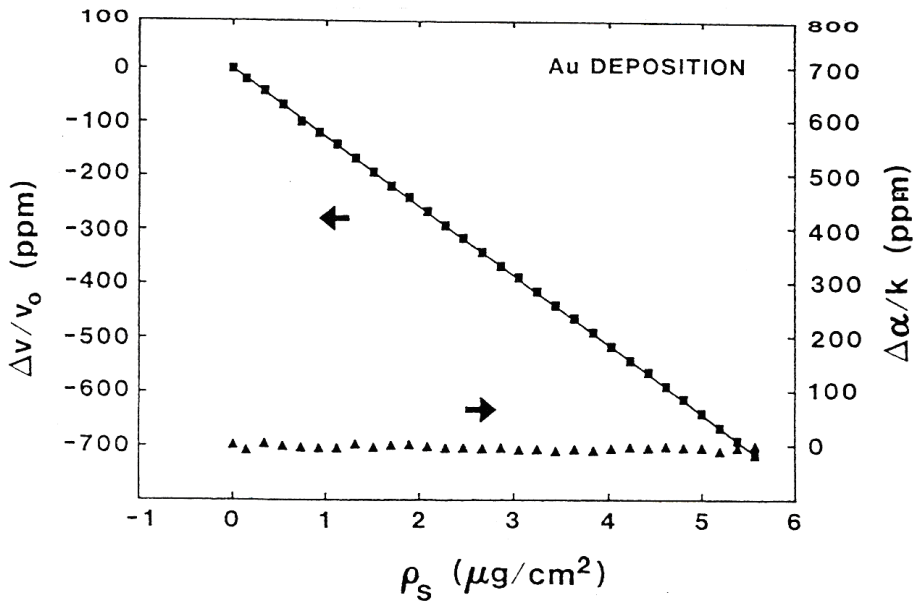


Figure 6: Fractional change in SAW propagation velocity and attenuation vs thickness of an evaporated metal film. Source: (Ballantine et al., 1997)

Acoustoelectric effect

When a SAW propagates in a piezoelectric material, it generates a layer of bound charge at the surface that accompanies the mechanical wave. This bound charge is the source of the wave potential ϕ and also generates an electric field. The equations which describes this interaction are given by:

$$\frac{\Delta v}{v_0} = -\frac{K^2}{2} \frac{\sigma_s^2}{\sigma_s^2 + (v_0 \sigma_s)^2} \quad (9)$$

$$\frac{\Delta \alpha}{\kappa} = \frac{K^2}{2} \frac{v_0 c_s \sigma_s}{\sigma_s^2 + (v_0 c_s)^2} \quad (10)$$

Where K^2 is the electromechanical coupling coefficient; σ_s is the sheet conductivity of the film; v_0 acoustic wave phase velocity; $c_s = \epsilon_0 + \epsilon_s$ is the sum of air and substrate dielectric permittivity (Jakubik, 2011)(Cheeke et al., 1999). These equations are plotted in figure 7. Consequently, the interdependence between the electrical potential associated with the acoustic wave and the carriers of the electric charge in the layer leads to a monotonically decrease in the velocity as sheet conductivity of the film increases while attenuation goes through a peak. The magnitude of the acoustoelectric response is proportional to K^2 , and is thus substrate dependent. The peak in attenuation, as well as the maximum rate of

velocity decrease, occurs at a critical sheet conductivity defined by $\sigma_s \equiv v_0 c_s$ (Ballantine et al., 1997).

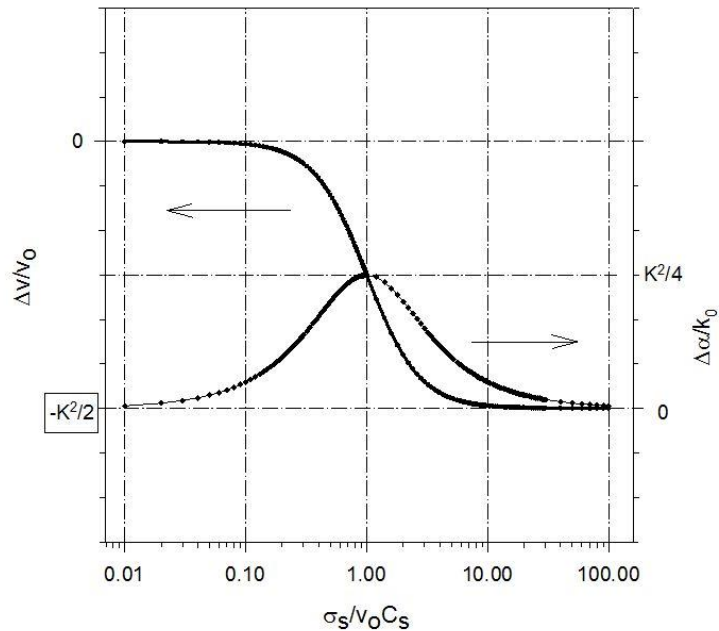


Figure 7: Acoustoelectric velocity and attenuation vs sheet conductivity

Chapter 2

Experimental

2.1 Deposition technique

Sputtering

There are many different ways to deposit materials such as metals, ceramics and plastics onto a surface (substrate) and to form a thin film. Among these is a process called “sputtering” that has become one of the most common technique to fabricate thin films and is the most popular method of physical vapor deposition (PVD).

Sputtering is based on the theory that particle to particle collisions will involve an elastic transfer of momentum, which can be utilized to apply a thin film to the substrate. In this technique, ions are accelerated toward a target by utilizing electric field. These ions are usually derived from either an ion gun or from exciting a neutral gas into ion plasma. As the ions are accelerated and bombard the target surface, they dislodge target atoms and other ions. The ejected atoms attach themselves to the substrate, and a thin film of the target material is produced (Kirschbrown, 2007). It is important to note that sputtering is preferred among other techniques due to its relative high deposition rates, good film properties and process stability (Wasa et al., 2012)(Suchea et al., 2006).

AC/DC Magnetron sputtering

In this plasma technique, magnetic field is used to enhance the plasma near the deposition source. DC sputtering begins with the ignition of a glow discharge or plasma through a large DC bias between a cathode and an anode under vacuum. In our case, high purity O₂ gas is inserted into the chamber for the oxidation of the

metallic Zn target into ZnO. When the oxygen ions collide with the target they will sputter a ZnO thin film onto the substrate's surface. If the bombarding particle's energy is high enough, it can either implant itself into the film, or it can transfer its momentum on a surface atom, causing it to re-sputter (Magnetics, n.d.).

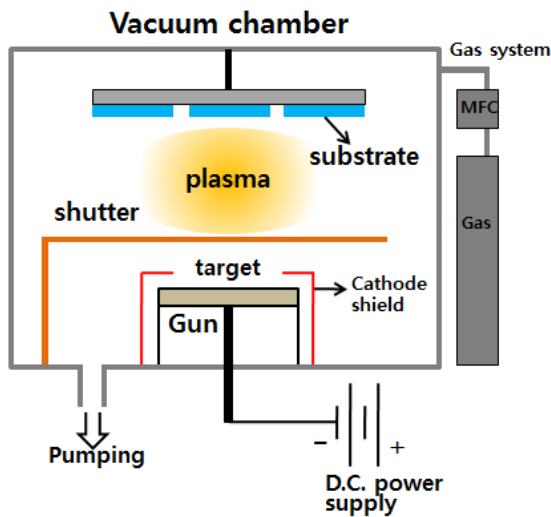


Figure 8: DC sputtering set up

Samples preparation

In this work, the deposition of the ZnO thin films was carried out in an Alcatel dc magnetron sputtering system using a 99.999% pure metallic zinc target. The base pressure of the ultra-high vacuum (UHV) chamber prior to deposition was under 3×10^{-6} mbar. The constant parameters of deposition were the total pressure 8×10^{-3} mbar, the substrate temperature at 26°C, the plasma current and voltage settings ($I=0.25$ Ampere and $V=280$ Volts respectively) and the sputtering atmosphere which consisted of 100% oxygen plasma. Films were deposited onto Corning 1737F glass with (25.4 ± 0.2) mm x (25.4 ± 0.2) mm dimensions and a thickness of (0.70 ± 0.07) mm. All Corning glasses were cleaned under sonication for 5 minutes with acetone and 5 minutes with propanol, then washed with distilled water and finally dried by N₂.

In the chamber for every sputtering run, a Corning glass with NiCr Ohmic contacts was used, for the conductivity studies, which were thermally evaporated in a UHV chamber to below 10^{-6} mbar. In addition Corning glass was also used, with Aluminum

tape for the measurements of the thickness, using an Alpha-step profilometer. The series was completed with SAW filters which were usable for sensing measurements.

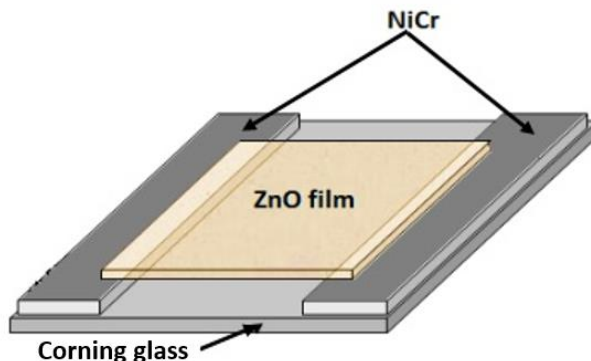


Figure 9: Geometry of the sample

The target of this study was the study of two sample series. The first one consisted of depositions of different thicknesses on Corning glasses with NiCr contacts for conductivity measurements and the second of different thicknesses on SAW filters and measuring the frequency shift. Concluding, the focus of this study was the sensitivity of ZnO thin films at room temperature, when exposed to ultra-low ozone concentrations, via conductometric and SAW measurements.

2.2 Characterization technique

2.2.1 Structural properties

X-Ray Diffraction (XRD)

X-Ray diffraction (XRD) relies on the use of X-rays to obtain information about the structure of crystalline materials. A primary use of the technique is the identification and characterization of compounds based on their diffraction pattern. Specifically with this technique one may measure the average spacing between layers or rows of atoms, determine the orientation of a single crystal or grain, find the crystal structure of an unknown material and obtain the size, shape and internal stress of

small crystalline regions. Generally it is preferred for the reason that is a nondestructive technique.

In this work the crystal structure of the deposited films was determined by X-ray diffraction (XRD) using a Rigaku RINT-2000 diffractometer with CuKa X-rays. The analyses recorded for 2θ values from 15° to 75° with a step of $0.05^\circ/\text{sec}$. The intensity of the beam was $I_0=20000 \text{ AU}$, the voltage was $V=40\text{kV}$ and the current $I=82\text{mA}$.

The dominant effect that occurs when an incident beam of monochromatic X-rays interacts with a target material is scattering of those X-rays from atoms within the target material. In materials with regular structure, the scattered X-rays undergo constructive and destructive interference. This is the process of diffraction.

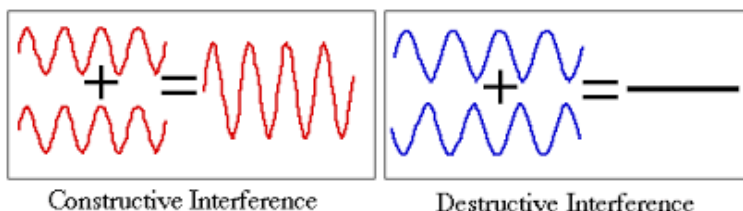


*Figure 10: Constructive & distractive interference wave. Source:
<http://www.reachoutmichigan.org/funexperiments/agesubject/lessons/bubbles.html>*

However it is important to understand the generation of X-rays. When an atom is bombarded with sufficiently high energy electrons, electrons are knocked out from their shell (excited state). This leads to transition of electrons to fill up the vacancy (ground state). Each electron transition generate X-rays of a specific energy equivalent to the difference of the transition shell energy. The diffraction of X-rays by crystals is described by Bragg's law:

$$n\lambda = 2d \sin \theta \quad (11)$$

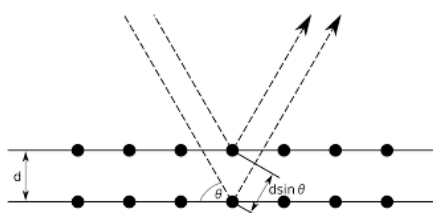


Figure 11: X-ray diffraction (Bragg's Law)

where d is the distance between atomic layers in a crystal, λ is the wavelength of the scattered X-ray beam, n is an integer and θ is the angle of incident beam.

The directions of possible diffractions depend on the size and shape of the unit cell of the material. The intensities of the diffracted waves depend on the kind and arrangement of atoms in the crystal structure. However, most materials are not single crystals, but are composed of many tiny crystallites in all possible orientations called a polycrystalline aggregate or powder. When a powder with randomly oriented crystallites is placed in an X-ray beam, the beam will detect all the possible interatomic planes. If the experimental angle is systematically changed, all possible diffraction peaks from the powder will be detected.

The lattice constant d for hexagonal structure, is calculated from the following equation:

$$\frac{1}{d_{(hkl)}^2} = \frac{4}{3} \left(\frac{h^2 + hk + k^2}{a^2} \right) + \frac{l^2}{c^2} \quad (12)$$

where h, k, l , are named Miller indices and (hkl) is the maximum reflection lattice plane and a, c are the lattice constants. Finally, for the estimation of grain size of the following Scherrer equation is used.

$$D = \frac{0.9\lambda}{B \cos \theta_B} \quad (13)$$

Where, λ is the X- Ray wavelength with a value of 0.154 nm, θ_B is the Bragg angle and B is the line broadening at half the maximum intensity (FWHM) in radians.

Scanning electron microscopy (SEM)

A scanning electron microscope (SEM) scans a focused electron beam over a surface to create an image. The electrons of the incident beam interact with the sample, producing various signals such as secondary electrons, backscattered electrons and X-rays that can be used to obtain information about the surface topography and composition of a range of organic and inorganic materials.

The main SEM components include:

- *Source* of electrons
- *Column* down which electrons travel with electromagnetic lenses

- Electron *detector*
- Sample *chamber*
- Computer and display to view the images

How it works

Electrons are produced at the top of the column, accelerated down and pass through a combination of lenses and apertures to produce a focused beam of electrons which hits the surface of the sample. The sample is mounted on a stage in the chamber area and both the column and the chamber are evacuated by a combination of pumps.

The most common SEM mode is detection of secondary electrons emitted by atoms excited by the incident electron beam. The number of secondary electrons that can be detected depends, among other things, on the angle at which beam meets surface of sample. By scanning the beam and collecting the secondary electrons that are emitted using a special detector, an image displaying the topography of the surface is created.

The maximum resolution obtained in a SEM depends on multiple factors, like the electron spot size and interaction volume of the electron beam with the sample. While it cannot provide atomic resolution, some SEMs can achieve resolution below 1nm. Typically, modern full-sized SEMs provide resolution between 1-20 nm whereas desktop system can provide a resolution of 20 nm or more.

2.2.2 Optical properties

Spectrophotometry (UV/Vis/NIR)

Spectrophotometry is the measurement of the reflection or transmission of a material or solution as a function of wavelength. It is one of the most useful methods of qualitative analysis in various fields such as chemistry, physics, biochemistry, material and chemical engineering and clinical applications.

A spectrophotometer is an instrument that measures the amount of photons, the intensity of light, absorbed after it passes through the sample. Depending on the range of wavelength of light source, it can be classified into two different type:

- **UV – visible spectrophotometer:** uses light over the ultraviolet range (185nm – 400nm) and visible range (400nm – 700nm) of electromagnetic radiation spectrum.
- **IR spectrophotometer:** uses light over the infrared range (700nm – 15000nm) of electromagnetic radiation spectrum.

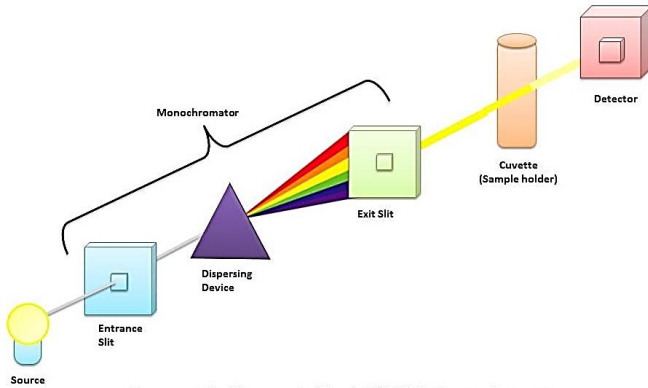


Figure 12: A simple UV/Visible spectrophotometer

Transmittance is defined as the ratio of the amount of light transmitted to the amount of light that initially fall on the surface,

$$T = \frac{I}{I_0} \quad (14)$$

Absorbance is defined as the negative logarithm of the transmittance, and note that absorbance and transmittance carries an inverse relationship. The equation below arises from Beer's law, $I=I_0 e^{-ad}$ and hence,

$$a = -\frac{\ln(T)}{d} \quad (15)$$

where d is the thickness of the film, a is the absorbance and T the transmittance.

As it is known, the direct transitions between the edges of a material with parabolic bands dependency of the absorption coefficient on the energy of incident photons ($h\nu$) is given by equation:

$$a(h\nu) = A^* (h\nu - E_g)^{1/2} \quad (16)$$

where A^* is a multiply constant and E_g is the energy gap of the material (Gagaoudakis et al., 2001). Consequently making the graph of a^2 with energy ($h\nu$) and adjusting a straight line in the area over the edge absorption, the energy gap of the studied material may be obtained from the intersection of this line with the energy axis.

2.3 Sensing techniques

Among the various gas sensing techniques available in this work we focused on the Conductometric (resistive) and surface acoustic waves (SAW) only. In effort to draw conclusions on their limitations on gas sensing (O_3) using the same sensing material (ZnO films).

2.3.1 Conductometric

The conductivity measurements were carried out in a homemade system representing in figure 13. The photoreduction process takes place at a pressure of 10^{-2} mbar and the samples were directly irradiated by UV light of a mercury pencil lamp with an average intensity of 4 mW/cm^2 at a wavelength of 254 nm, placed at a distance of approximately 3 cm from the surface of the film. For the subsequent oxidation process ozone was produced by an ozonator (Thermo Electron corporation, model 49i) at different concentrations between 5-2400 parts per billion (ppb) and the chamber was backfilled with oxygen and ozone at a pressure of 100 mbar. This treatment lasted for several minutes ranging from 8-15min, depending on the thickness of the samples, after which no further changes of the conductivity could be observed. Finally, the chamber was evacuated and the photoreduction-oxidation cycle was repeated at the next concentration level.

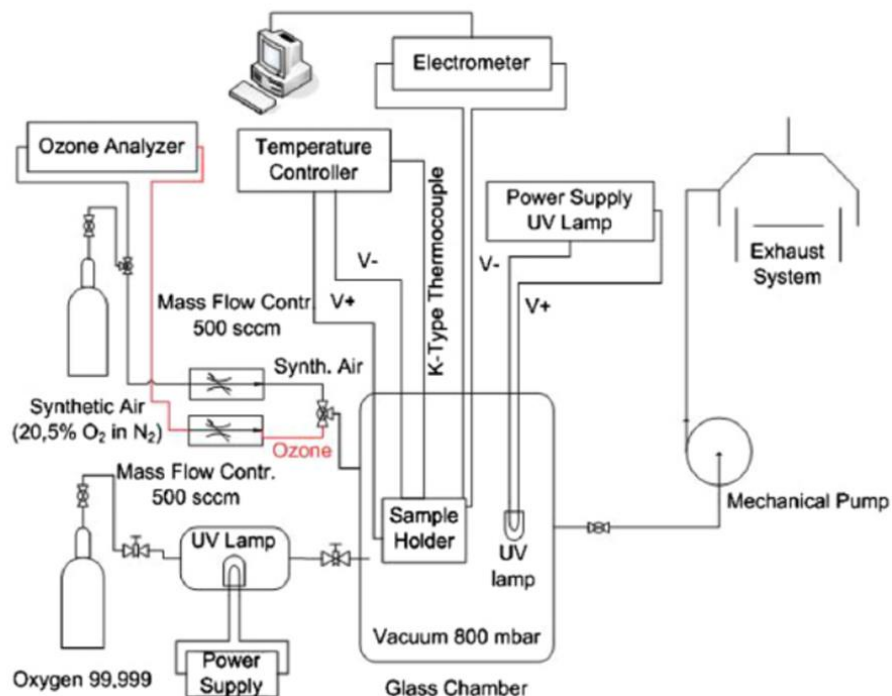


Figure 13: Schematic of conductivity-based system for photo-reduction and oxidation processes. Source: (Kiriakidis et al., 2012)

In order to measure the electrical changes of the film during the photoreduction-oxidation procedure, constant voltage was applied during the whole cycling procedure to the samples and the electric current measured by a Kiehley 6517A electrometer. Eventually the conductivity was calculated by the following equation

$$\sigma = \frac{I}{V*t} \quad (17)$$

Where, t is the thickness of the deposited film and V is the applied electric field. The units of conductivity are $(\Omega\text{cm})^{-1}$.

Photoreduction – Oxidation

It is known that the basic mechanism of gas detection is the interaction of the gaseous species with the surface of the semiconducting sensitive metal oxide layer (Kiriakidis et al., 2012)(Batzill et al., 2004). This sensing mechanism can be explained by production and charge transfer processes of electrons (e^-) and holes (h^+) on the surface of the thin film (ZnO , in our case). In other words, the conductivity changes

explained by the formation and annihilation of oxygen vacancies at the metal oxide surface. UV irradiation of the samples with energy higher than the bonding energy between Zn and O leads to the transformation of an oxygen atom from a bound state to the gaseous state and thus the creation of charged oxygen vacancies at the metal oxide surface. Therefore, an increase in the free electron concentration occurs resulting in an increase in conductivity. Subsequent exposure to oxidizing gas, such as O_3 , leads to annihilation of the charged oxygen vacancies on the surface and, hence to a drastic decrease of the carrier concentration. That leads to an increase of the resistance and consequently the decreasing of the conductivity, which can be used as the sensor signal (Kenanakis et al., 2007) (Wei et al., 2011).

2.3.2 Surface acoustic waves

The second technique for sensing measurements applied in this work was the surface acoustic waves. The aim of this technique was to investigate the operational limitations of these commercial filters. The sensing material, ZnO, were deposited via sputtering, as mentioned above, onto commercial SAW filters with operating frequency of 930MHz with different thicknesses (similarly to Conductometric measurements). For the deposition of the sensing material, the top of the filter was removed cautiously, in order to avoid the damage of the interdigital transducer structure. Then the SAW devices were mounted on a micro-heater in a Teflon based gas chamber, approximately 30 ml in volume (see fig. 14). Using a computerized multi-channel gas calibration system, each device was exposed to a sequence of O_3 gas pulses. The exposed O_3 gas concentrations range was from 110 ppb to 2 ppm approximately. All the measurements were taken at room temperature conditions. For the photoreduction a UV pencil lamp was used, located above the cell opposite the SAW filter, providing simultaneously nitrogen (N_2) flow. The existence of N_2 serves to maintain stable experimental conditions, especially on temperature and O_3 presence, because the UV lamp is expected to affect them. The gas flow rate was kept the same at 500ml for both processes and during all cycles. A labview based

program was used to facilitate automatic computer calculations, giving data of time, central frequency and attenuation.

All the characteristics of the commercial (Golledge) filters that used for the experiments are given in the appendix I.

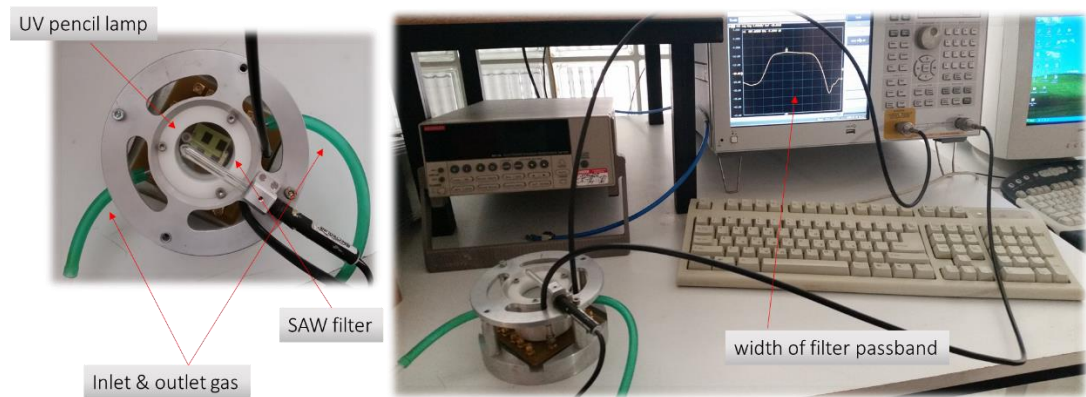


Figure 14: Home-made cell hosting SAW filter

Chapter 3

Results

3.1 Characterization Techniques

Structural characterization

XRD

Figure 15 reveals ZnO XRD patterns from thin films produced at different deposition times. The thicknesses vary from 30 to 230 nm. It becomes apparent that as the thickness increases, the peak intensity at $2\theta \approx 34^\circ$ corresponding to (002) plane increases. So the films grow preferentially along c-axis orientation, vertical to the substrate, which is something expected from previous studies (Ayouchi et al., 2003)(Bedia et al., 2014)(Tseng et al., 2015).

The obtained diffraction patterns were well compared with the Joint Committee on Powder Diffraction Standards (JCPDS card no. 36: 1451) and are indexed as hexagonal wurtzite zinc oxide, without any impurities. Higher crystallinity has been met for thicker samples. The sample with thickness 30 nm is amorphous therefore diffraction peaks are missing.

Moreover, crystallite size of the samples was calculated using the Debye – Scherrer's formula, equation (11) and is being presented in Table 2.

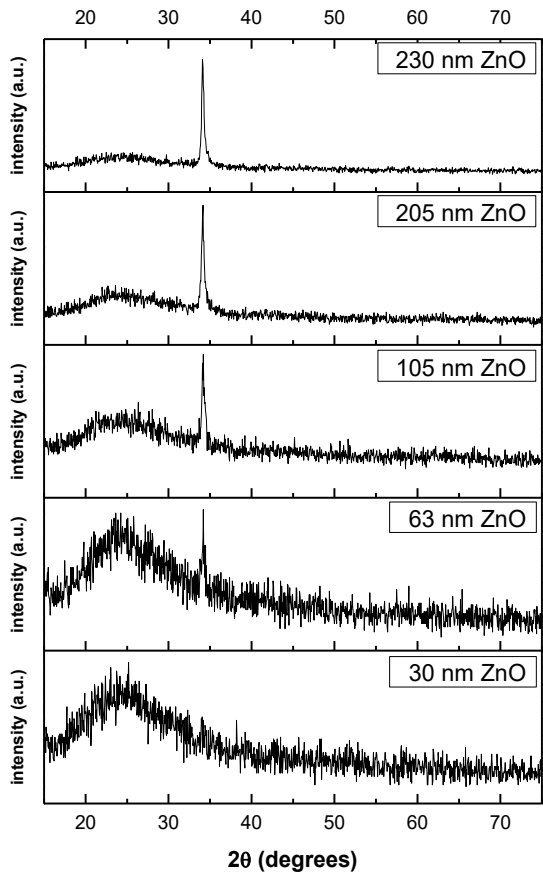


Figure 15: XRD pattern of ZnO thin film deposited at different deposition rates

SEM

In the following pictures cross-sectional SEM images are presented. The thickness of the samples obtained via this technique is in good agreement with the value that was obtained by the alpha-step profilometer.

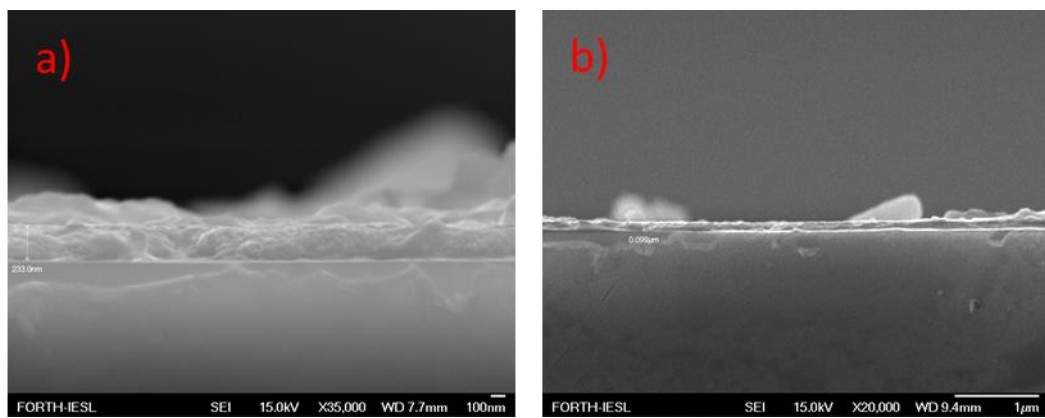


Figure 16: Cross-sectional SEM image of ZnO thin film a) 230 nm & b) 105 nm

Optical characterization

Figure 17 shows the spectrum of optical transmittance for wavelength range $\lambda = 250$ - 2500 nm. At this spectrum the transmittance T (%) is presented for all samples including Corning glass (substrate). It can be seen that, all samples exhibit a high transparency above 80% with a maximum value in visible and the near infrared region. These results are in a good agreement with other studies (Jin et al., 1994), (Musat et al., 2008). For thicker films, specifically above 200 nm fringes were present, attributed to the effect of internal scattering.

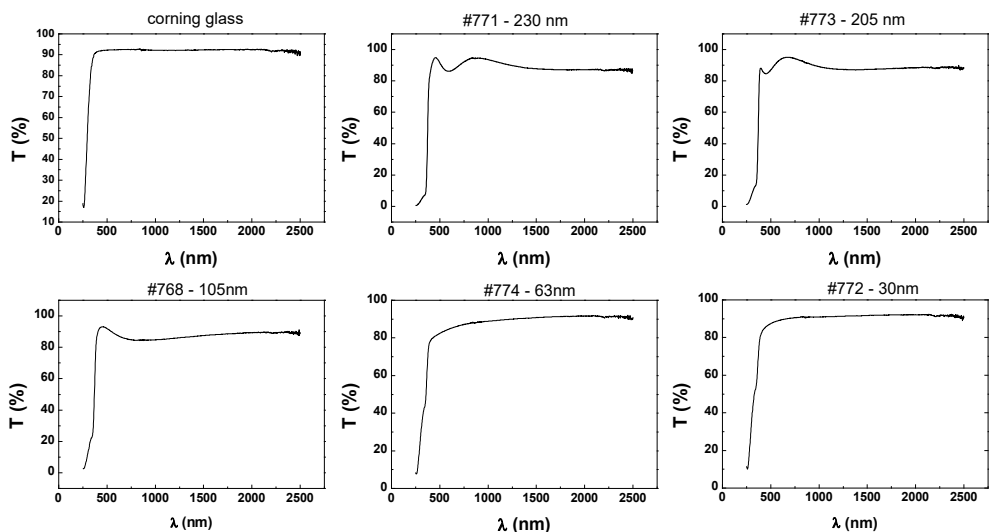


Figure 17: Transmittance spectra of ZnO thin films

Furthermore, in figure 18 a plot of the optical band gap and grain size as a function of thickness is shown. The optical energy gap of ZnO films is calculated from equation (14), as described in paragraph 3.2.2, and was found to range from 3.30 – 3.32 eV which is in a good agreement with previous studies (Suchea et al., 2006), (M. Bender et al., 2002), (Kenanakis et al., 2007).

Hereby, Table 2 lists the overall structural results acquired from the characterization techniques.

Table 2: Structural results

| Sample | Thickness (nm) | Optical band Gap, Eg (eV) | Grain size D (nm) | d-spacing (nm) |
|--------|----------------|---------------------------|-------------------|----------------|
| #771 | 230 | 3.30 | 15.096 | 0.262 |
| #773 | 205 | 3.32 | 13.209 | 0.262 |
| #768 | 105 | 3.31 | 13.519 | 0.262 |
| #774 | 63 | 3.30 | 6.288 | 0.263 |
| #772 | 30 | - | - | - |

Grain size, optical band gap and d-spacing are being presented. An increase in grain sizes is observed with increasing film thickness (Bhasker Raj et al., 2013) whereas d-spacing remains relatively stable. This is expected since the diffraction angle at (002) peak for all the samples is similar, therefore from Bragg's law (equation 11), keeping the wavelength stable, there is stability in the interplanar spacing (Lin et. al., 2005).

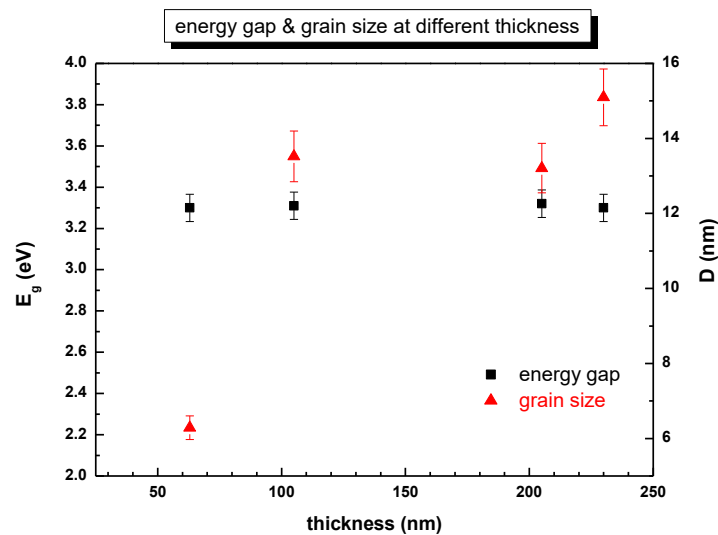


Figure 18: Energy gap & grain size as function of thickness

3.2 Sensing

Conductometric

In this session the variation of conductivity under exposure to 5 different ozone concentration levels as well the normalized exponential decay curves as a function of thickness are being presented, ranging from 230 nm down to 30 nm.

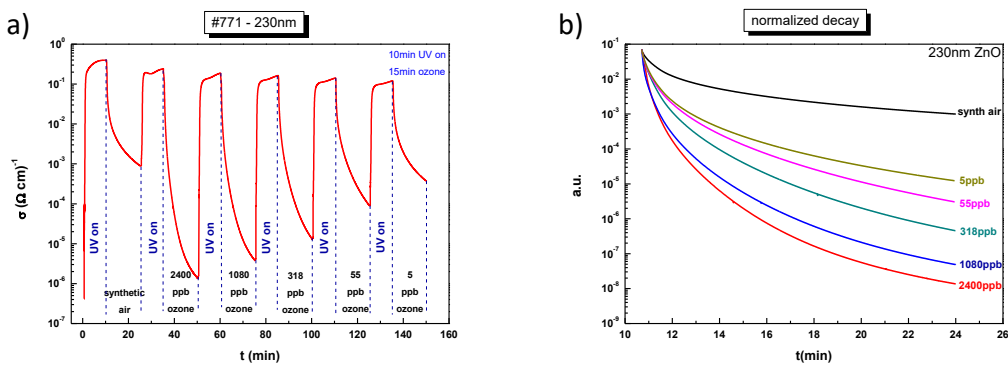


Figure 19: a) Photoreduction-oxidation process of ZnO film 230nm,
b) Normalized exponential decay curves of 230nm

For the thicker sample (230 nm) the photoreduction process lasted 10 min and the oxidation 15 min. From the graph in figure 19a it is observed that the conductivity is ranging from 10^{-6} to $10^{-1} (\Omega \text{ cm})^{-1}$ approximately; resulting to a 5 orders of magnitude response, making this sample a highly sensitive ozone sensor. It is important to note that in each photoreduction cycle the maximum conductivity values remain almost constant for all concentration levels. However, the response in the oxidation state was found to be a function of the concentration levels with the response getting smaller. This is something expected and desirable, since sensors must show a higher response at different higher concentration levels and vice versa.

Figure 19b depicts the normalized decay curves obtained from the oxidation processes and starting from the same point. The slope of every curve represents the ability of the sensing material, in this case ZnO of 230 nm, to sense the different

ozone concentration levels with adequate resolution even from the first minute of exposure.

Results for the sample of 205 nm is shown in figure 20, with the photoreduction process again lasted 10 min and the oxidation 15 min. As it can be observed, the sample appears to have similar behavior as previously. The highlights of the sample would be its good response, high sensitivity and distinction of different ozone levels.

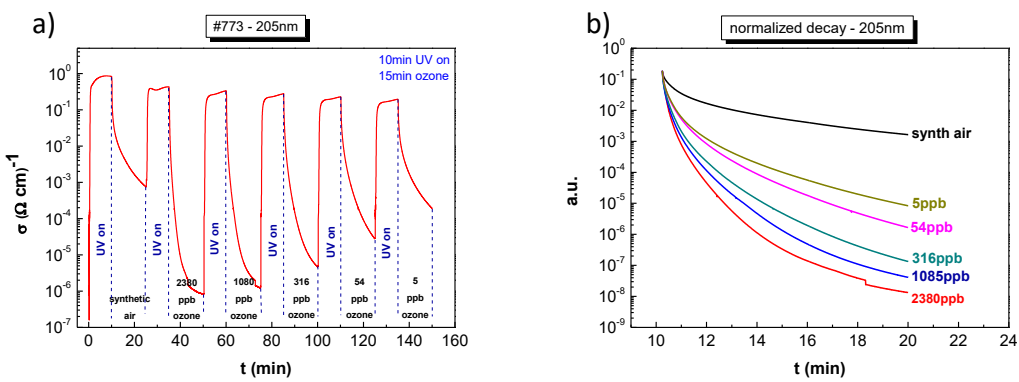


Figure 20: a) Photoreduction-Oxidation process of ZnO film 205nm,
b) Normalized exponential decay curves of 205nm

Nonetheless for films with much lower thicknesses as in the case of the 105 nm sample, although it seems to have a good response, specifically 3 orders of magnitude (fig. 21, a), the response to all ozone levels concentrations could not be adequately distinguished exhibiting a poor resolution between the different ozone concentrations levels being introduced. This becomes apparent when observing the corresponding normalized decay graphs (fig. 21, b). This behaviour could be attributed to the specific film growth and/or testing conditions and may be regarded as an artifact of the present study.

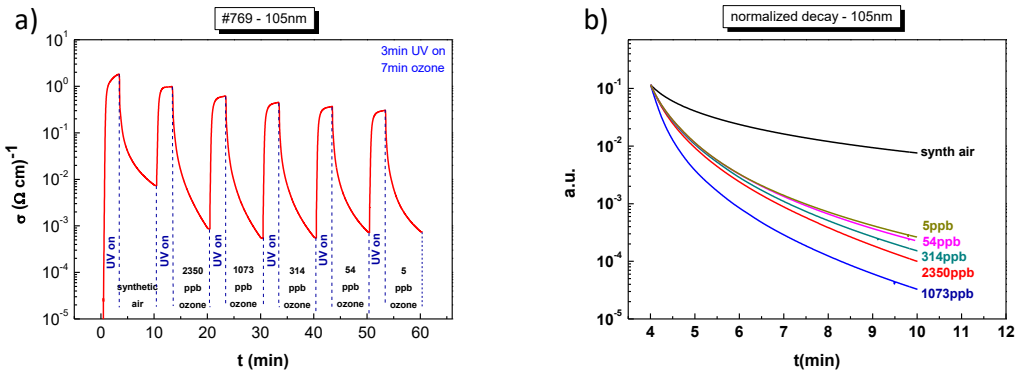


Figure 21: a) Photoreduction-Oxidation process of ZnO film 105nm,

b) Normalized exponential decay curves of 105nm

Results for the sample of the lowest thickness (63 nm), with photoreduction lasted 3 min and oxidation 12 min, are shown in figure 22. Even at this thickness, the sensitivity is good and corresponds to 5 and 4 orders of magnitude overall throughout all concentration levels. However, the exponential decay curves show that it is not possible to differentiate the ozone levels except when it comes to the point of recognizing the difference between the levels of thousand ppbs to the unit levels. It can be easily observed that in this case there is a good distinguish at decade levels and lower; therefore this thickness is considered to be a good candidate for detection in ultra-low ozone concentrations levels.

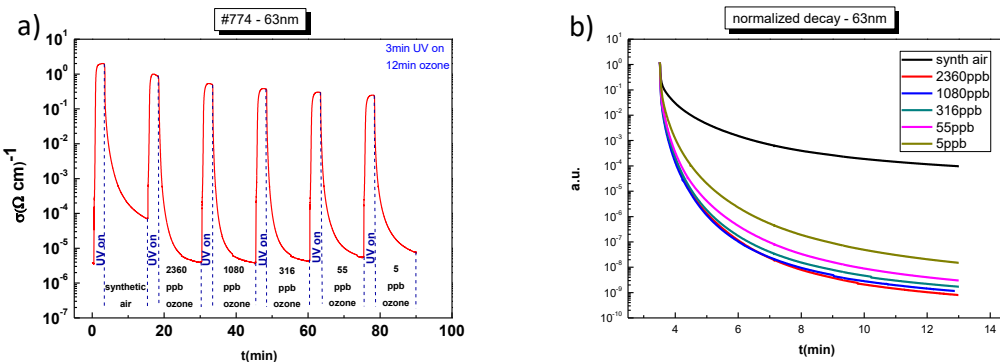


Figure 22: a) Photoreduction-Oxidation process of ZnO film 63nm,

b) Normalized exponential decay curves of 63nm

Finally for the thinnest sample of 30 nm, photoreduction lasted 2 min and the oxidation process 8 min. The response is approximately 3 and 2 orders of magnitude as ozone concentrations are decreasing (fig. 23, a). Again the behavior of

the exponential decay curves (fig. 23, b) were exactly the same with those of sample of 63 nm providing us with similar results.

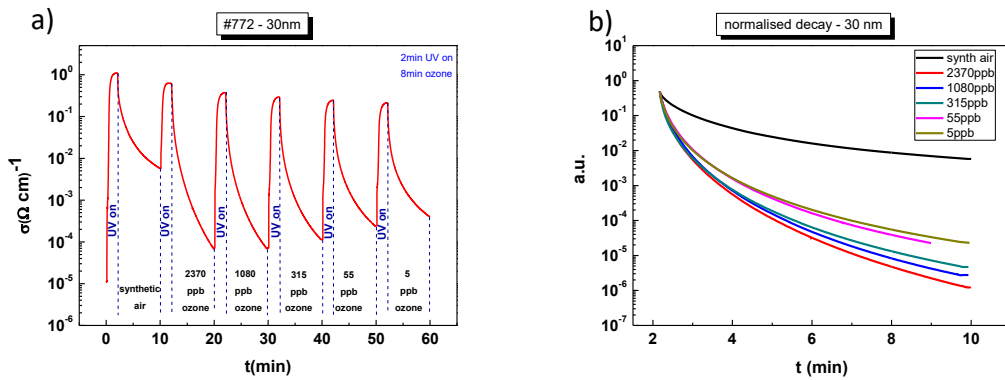


Figure 23: a) Photoreduction-Oxidation process of ZnO film 30nm,
b) Normalized exponential decay curves of 30nm

Sensitivity analysis

The sensitivity was calculated from the ratio of the maximum to minimum conductivity values, as shown in the following formula:

$$S = \frac{\sigma_{\max}}{\sigma_{\min}} \quad (18)$$

The change of sensitivity as a function of concentration levels for the different thicknesses, is presented in figure 24.

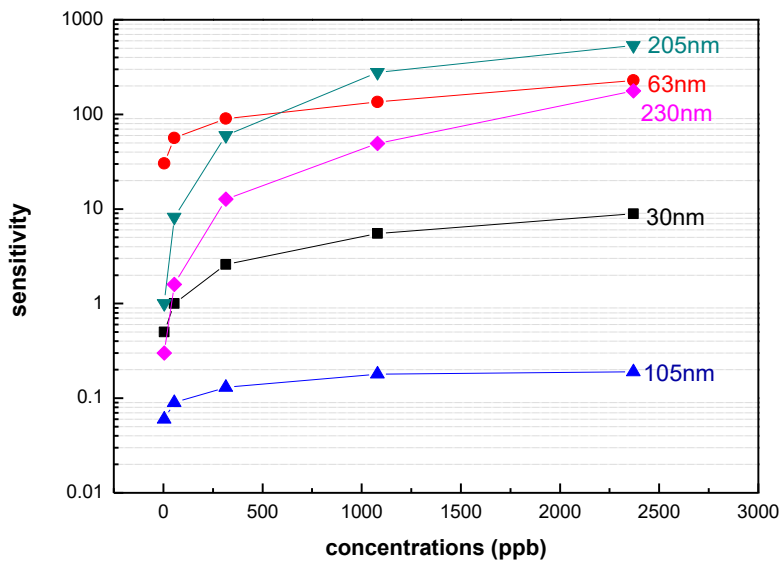


Figure 24: Sensitivity as a function of concentration for all thicknesses

For concentrations over 1000 ppb the sensitivity for almost all films remained constant and the variations are within one order of magnitude. This denotes the films inability to safely differentiate O₃ concentrations in this high volume range. On the contrary, for ozone concentration levels less than 500 ppb the variations are obviously larger, implying that the sensing material can detect and distinguish very low ozone levels at the low thickness range.

Stability – Repeatability

As a concluding remark, a repeatability and stability test has been added in this sector. For this test, the sample of 205nm thickness has been selected. During this repeatability test three consecutive photoreduction – oxidation cycles were tested, at 1200ppb of ozone concentration. All the experimental conditions were kept exactly the same during the whole experiments. It is apparent from figure 25, that this sample has the same response to every cycle exhibiting good repeatability, thus it can be used as a sensor reliably.

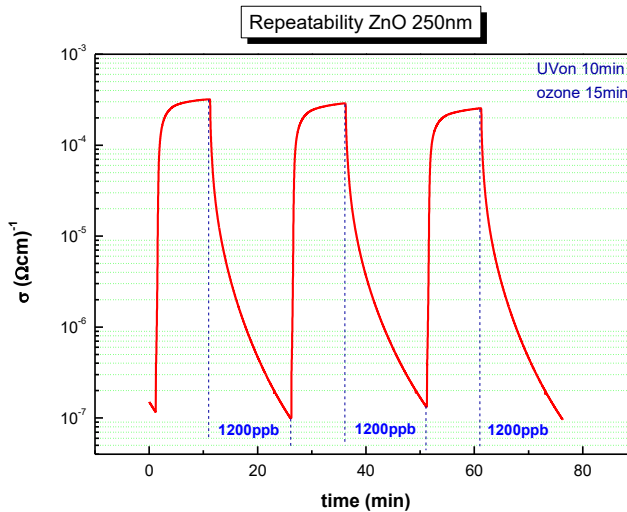


Figure 25: Repeatability of ZnO 205nm thickness

In order to test the stability of the aforementioned sample, the repetition of the experiment took place 3 months after the first test, keeping stable conditions as prior. The comparison of the two periods with 3 months difference, is shown in figure 26. The response to every cycle after 3 months became approximately 2

orders of magnitude less. This results in an unexpected reproducibility which means that the device cannot be used after a short period of time. This might be attributed due to the oxidation that has undergone from the ambient atmosphere because the samples were not kept in sterile and completely clean environment.

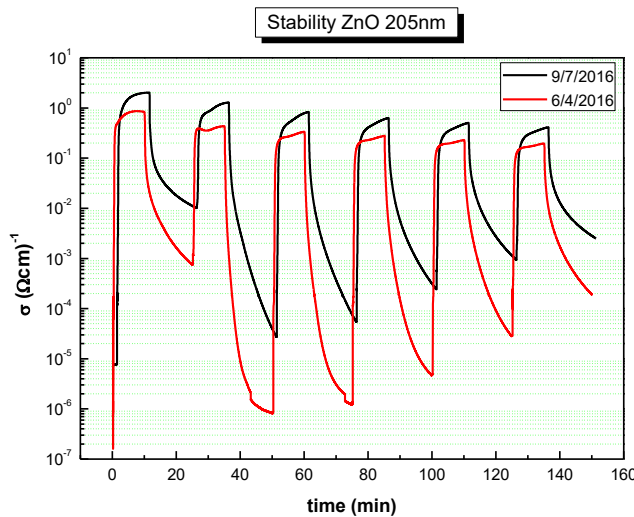


Figure 26: Stability of ZnO 205nm after 3 months

Analysis

Taking into account all the above measurements, further analysis of the results will be presented in this section. In the process of photoreduction the oxygen bonds crack and create oxygen vacancies releasing two electrons for each missing oxygen. In the subsequent process of oxidation by the presence of the O₃ the sensitivity of the thicker samples seems to decrease with the decrease of ozone concentration levels. Consequently the response is higher in higher concentration levels (Huang et al., 2011). This happens due to the fact that the oxygen vacancies of the film are not fully occupied by the oxygen molecules of the ozone, during oxidation process, so when increasing the ozone concentration levels the response is higher. However when it comes to thinner samples the oxygen vacancies are initially occupied directly from the first ozone concentration levels, during oxidation process leading to fast saturation. This behaviour is repeatable in every photoreduction-oxidation cycle (M. Bender et al., 2002).

Obviously gas sensors are not activated without the presence of UV light. This is in good agreement with the literature, since chemisorbed oxygen of the metal oxides is thermally stable at room temperatures (de Lacy Costello et al., 2008).

Collectively, differences in the exponential decay curves are apparent, denoting the dual ability of ZnO thin films to both monitor and separate the various ozone concentrations down to the very low level of 5 ppb. In addition, this allows resolution of these responses from those of the synthetic air, used as the reference signal.

Comparing our results with the open literature, the conductivity and gas sensitivity increased with the increase of the grain size (de Lacy Costello et al., 2008), and consequently with the increase of the thickness.

Results deriving from the experiments on the repeatability and stability, show high repeatability, coming into good agreement with the literature (Kim et al., 2015) (Chien et al., 2010). However, when stability is taken into account, the results of this research are contradicting with the results of former studies which appear to have much higher stable performance. Even higher stability is found in other metal oxides, like InO_x which show a high stability even after 7 years (Binas et al., 2016).

The gas sensors deposited in this research have up to 5 orders of magnitude response. Several studies have been made with ZnO gas sensors, via sputtering at room temperature achieving 8 orders of magnitude (M. Bender et al., 2002) and 7 orders (Kiriakidis et al., 2012). However most of the research studies use chemical techniques for the growth of ZnO namely spray pyrolysis giving a response of 3 orders of magnitude (M. Bender et al., 2002), dip-coating technique resulting at 2 orders of magnitude (Cheng et al., 2004) and sol gel dip coating giving a response of an order of magnitude, Chemical vapor deposition (CVD) achieving just 2 orders of magnitude, and aqueous solution method providing a response at an order of magnitude at various oxidizing gases have been reported (Huang et al., 2011). Overall, compared to literature, the sensors deposited in this research study, are high sensitivity sensors, activated at room temperature and low ozone concentrations.

Surface acoustic waves (SAW)

At this last section, the operating limits of commercial SAW filter of 930MHz by depositing different sensing material thicknesses are presented. Consequently, the test measurements which will bring out the operational limits, will be firstly presented, thereafter a test measurement which ensure the reliability of all measurements will be cited and finally the contribution of the two main interactions mentioned in Chapter 1 will be further investigated.

Operating limits

To investigate the operational limits of the 930MHz SAW filter, the central frequency of the filter without sensing material on the top was initially measured. After that, onto the same filter, ZnO was deposited for various deposition times, resulting to different thicknesses. From the plots of amplitude and phase, depicted in graph 27 a & b, the critical mass from which onwards filters bandpass breaks down is observed. From this procedure the operational limits of the filter can be defined.

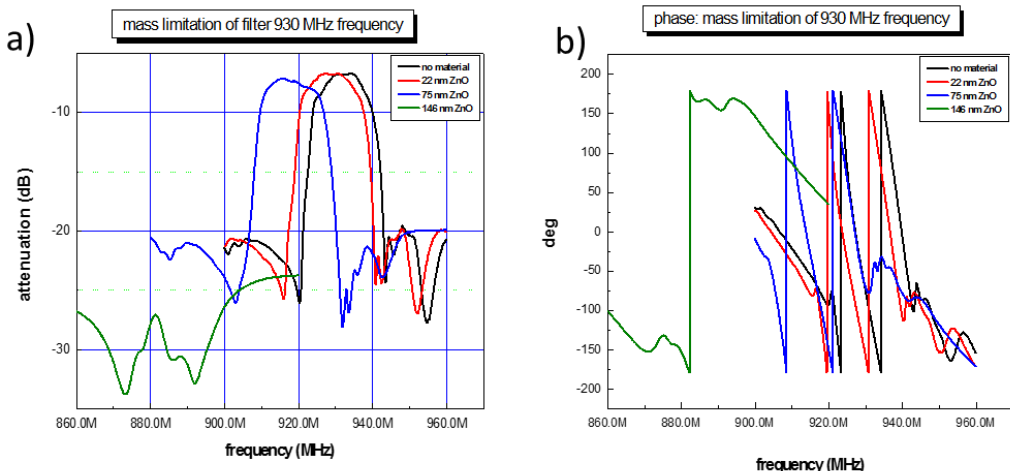


Figure 27: a) Frequency shift, b) Phase shift due to ZnO deposition

As expected, with the addition of mass a shift of frequency to lower values occurs. This phenomenon is expected and will be explained by the following measurements. Therefore it is extracted from these plots that the filters can operate with a limiting presence of thin film mass on their top until the deposition thickness of 80nm approximately. With further mass addition, the bandpass functionality of the filter clearly losses its form, so it can no longer be used as a sensor. Exactly the same

conclusion can be drawn from the phase plot of the transmitted signal as a function of the excitation frequency. The two peaks indicate the two frequencies oscillating with less insertion loss and a round-trip phase shift of zero.

It is important to note that this experimental procedure was performed for one more filter with the same nominal frequency at the same sputtering run, in order to keep the same conditions during this work, and the result was the same with the above (appendix II).

Measurements reliability

In order to ensure that all sensing measurements were accurate and every observed shift of the oscillating frequency was due to the presence of the sensing material, one more test measurement took place. A filter with nominal frequency 930 MHz with the absence of the sensing material (ZnO) was used. The procedure was as follows: at first the sample was illuminated with a UV lamp for 5 minutes and then exposed to the testing oxidizing gas (ozone) for 5 more minutes. All results had shown that there was no detectable change at the oscillating frequency and thus the experiments could be carried out reliably.

Influence of sensing layer on the SAW operation

With respect to the presented theory (Chapter 1, mass loading) all the responses that occur with addition (or removal) of areal/mass on the surface of a sensor are due to changes of the wave velocity.

The following figure 28 depict the frequency response of SAW filters of 930 MHz before and after deposition of the sensing layer with different thicknesses. With the red line the filter before sputtering is presented and with the black line after sputtering, starting from thinner to thicker films. Specifically, at this study only three thicknesses (30nm, 63nm & 100nm) were tested due to the operational limitation, as discussed above.

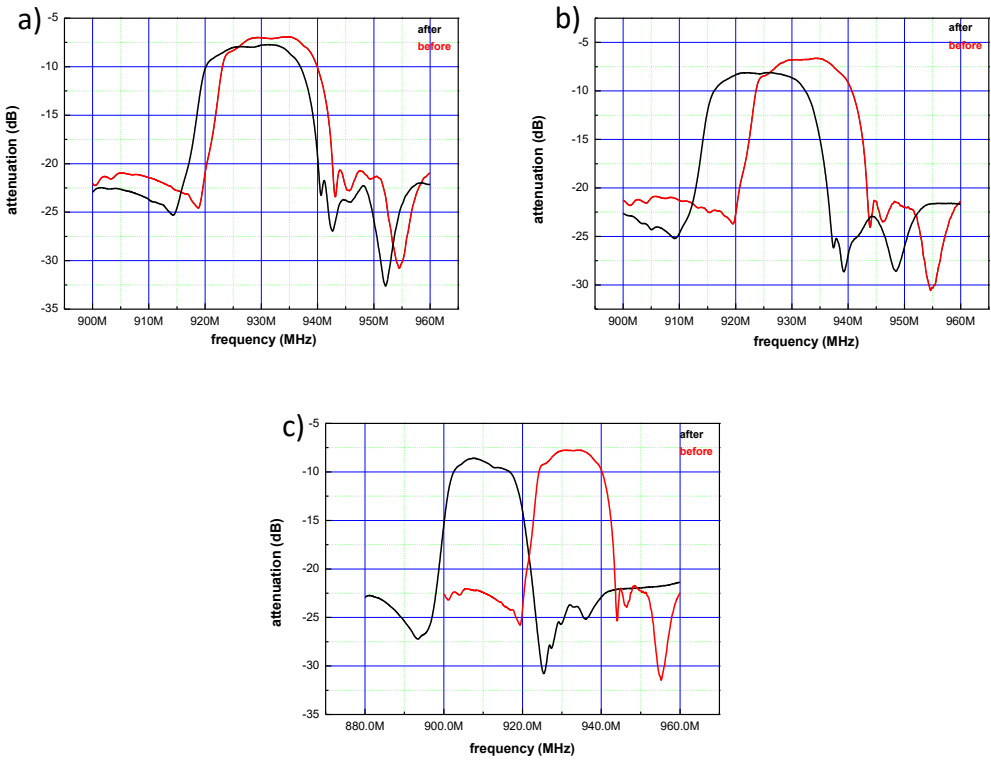


Figure 28: Frequency shift due to sensing layer deposition, a): 30nm, b): 63nm & c): 105nm

It is apparent that a small shift at lower frequencies occurs by adding mass with no noticeable changes to attenuation observed (Cheeke et. al., 1999). This happens, as explained, because an increase in the kinetic energy density (due to the wave movement on the surface) results in a decrease in wave velocity. Consequently, from equation 8, the fractional velocity change varies with operating frequency f_0 and decreasing linearly with the surface mass density (Figure 30).

On table 3 results from previous graphs are displayed, in which the nominal frequencies (before sputtering) and the shifted (after sputtering) as well and insertion losses have been recorded respectively. From now on, the shifted frequency will be considered as the central frequency for detecting future acoustic wave velocity variations.

Table 3: Recorded frequency & insertion loss

| Thickness (nm) | Nominal frequency (MHz) | Central frequency (MHz) | Frequency variation Δf | Nominal insertion loss (dB) | Central insertion loss (dB) | Attenuation Variation Δa |
|----------------|-------------------------|-------------------------|--------------------------------|-----------------------------|-----------------------------|----------------------------------|
| 30 | 934.70 | 930.91 | -3.79 | -6.91 | -7.75 | -0.84 |
| 63 | 934.03 | 925.89 | -8.14 | -6.63 | -8.10 | -2.31 |
| 105 | 930.59 | 907.42 | -23.17 | -7.56 | -8.58 | -1.02 |

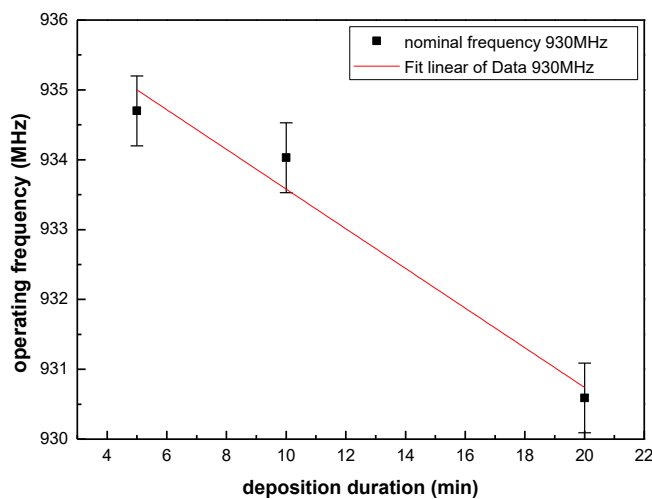


Figure 29: Operating frequency dependence vs ZnO deposition duration

The effect of acoustoelectric response to sensing mechanism of SAW

In addition to mass loading results, SAW filters responses were tested toward oxidising gas (O_3) with varying concentrations at room temperature, in order to examine their acoustoelectric behaviour.

In the following graphs the centre frequency variations towards consecutive photoreduction and oxidizing cycles against four different ozone concentrations is presented. Every cycle lasted 15min, of which 5min was for the photoreduction and 10min for the oxidation process. As mentioned before, the last process lasted twice as long because of the fact that this is a slower process.

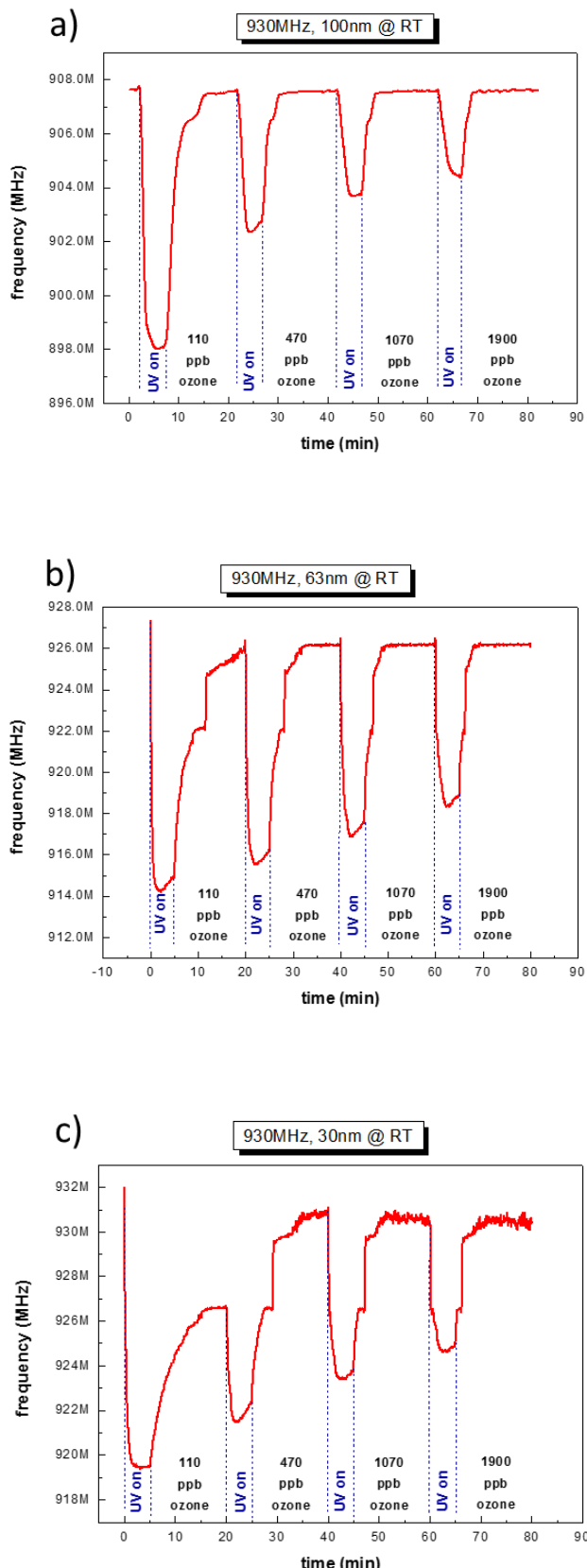


Figure 30: 930MHz SAW filter response toward different O_3 concentrations at RT a) 105nm, b) 63nm, c) 30nm

From the above results the theoretical predictions for decreasing central frequency under the UV illumination and reversible increases upon exposure to the test gas were confirmed. This result is in a good agreement with the literature (Kiriakidis et al., 2012)(Ippolito et al., 2005)(Matatagui et al., 2015) using also other oxidizing gases such as NO₂. In more detail, in line with the conductometric measurements, upon exposure to oxidizing gas, it was confirmed that the conductivity decreases. It is well known that when n-type metal oxides such as InOx and ZnO are exposed to oxidizing gas, oxygen molecules are adsorbed on the surface. The adsorbed molecules extract electrons from the conduction band and an electron– depletion region is created extended from the surface, the result of which is the increase of the sensing film resistance therefore a decrease of its conductivity (Ahn et al., 2013). Consequently for SAW sensors, in line with equation 9 which combines the wave velocity and the sheet conductivity, it is expected that a decrease in the sensing film conductivity results to the velocity increase. Therefore combining this with equation: $f = v * \lambda$, in which velocity and frequency are directly proportional, an increase of frequency is expected. Our results confirm such a dependency and coincide perfectly with theoretical predictions and past experimental data on oxidizing and reducing gases utilizing metal oxides as gas sensing elements (Bhasker Raj et al., 2013).

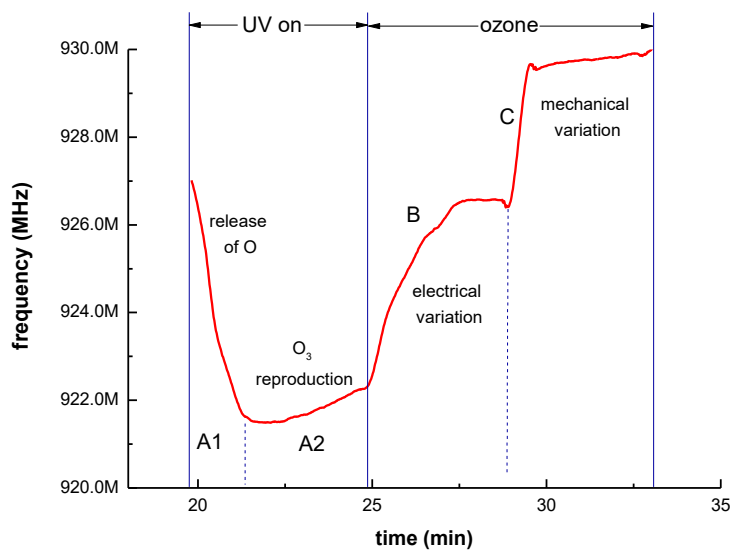


Figure 31: Detailed representation of photoreduction-oxidation procedure through SAW device

Analysing our results in more detail , it has been observed (fig. 30) that the initial response of our SAW filters following the deposition of the sensing material with thicknesses ranging from 30 to 100nm is shifted by 8-9 MHz for all the samples. This is the result of mass loading and is justified by the fact that the sensing material (ZnO) is highly insulating i.e. induces no inherent acoustoelectric effects. . Following subsequent analysis applying cycles of photoreduction and oxidation, a drift of the base line frequency was noticed denoting an increasing memory effect of the oxidation state. Specifically, as the concentration increases the measured frequency gets higher. This is explained by the fact that the more ozone is induced in the chamber, the more coverage of the vacancies sites is achieved, resulting to an excess of oxygen at the surface sites. This means that when the photoreduction process starts again the process needs more time for full surface reduction and if this is not available, as in our case, than an unspecified amount of oxygen adsorbed during the previous cycle remains on surface active sites (fig. 31, region A1). Needless to say that repeatability tests under the same ozone concentration, analyzed in the following section, did not show any of the above memory effect.

Continuing the analysis of the obtained results we have observed that, after several seconds and while the samples are illuminated by the UV lamp, a frequency increase was taking place (fig. 31, region A2). This was attributed to the fact that prolong exposure of the film to the UV light in an environment that is not a very good vacuum and thus there are oxygen molecules besides and during photoreduction an oxidation process takes place. This oxidation starts at this point when oxygen molecules are exposed to UV and then ozone is produced (Martins et al., 2004) and this creation of ozone molecules leads to a reactive process that competes with that of reducing under UV. Subject to the strength and amount of oxygen presence, a different slope appears, which becomes slightly smaller with the increase of O₃ concentration, and this can be attributed to above phenomenon.

Further analysis of the obtained data and in addition to the above, taking a more careful look at the graph (fig. 30) ranging from thinner to thicker samples, it can be easily concluded that during the oxidizing process a two-step procedure takes place. This procedure is more intense on the filters with the thinner sensing layer; whereas

as the thickness increases, this effect slightly declines. Specifically, the region which is marked as B in figure 31 presents the first step and can be attributed to the acoustoelectric effect, as discussed in detail at the above paragraphs. This behaviour corresponds exactly to the results from the conductometric response analysed earlier, as a result of surface phenomenon. It must be emphasized, that this step stops at the same value of frequency, independent of the concentration, denoting it is a surface phenomenon. Gas sensing is a surface dominating phenomena, therefore the thickness of the sensing layer on the surface of SAW device is expected to play a crucial role in the response characteristics of SAW sensor. In the work of Bhasker Raj et al., 2013, various metal oxides were studied, ZnO sensing layer exhibit the maximum response. At the obtained graphs, mass loading and elastic loading identified as the major contributions towards the response of SAW. The first (mass loading) causes a decrease in frequency whereas the other an increase. The second step, which is marked as C in figure 31, it is believed to be related more to a mechanical phenomenon related to the nature of the SAW transducer used as substrate rather than a pure acoustoelectric one. Supporting evidence on the argued explanation is the fact that no such behaviour has ever been reporting on metal oxide sensing layers deposited on other rigid or flexible substrates. Thus, it is believed that this is a phenomenon related to the mechanical properties of the used substrate i.e. it is directly related to the elasticity of the piezoelectric substrate. Such a change of its mechanical properties may be attributed to the interaction between O₃ with the structure of SAW that leads to changes to its elasticity (Young's module).

It is well known that the piezoelectric materials couple electrical and mechanical effects and also thermal effects, thus they are sensitive to a large number of parameters (N. Nakamura et al., 2012). These are usually described by the relations,

$$T = c^E S - eE \quad (19)$$

and

$$D = \varepsilon^S E + eS \quad (20)$$

in which T is the mechanical stress (Nm⁻²), c is the stiffness with constant electric field, S is the mechanical strain, e is the piezoelectric stress constant (Cm⁻²), E is the

electric field (Vm^{-1}), D is the electric displacement (Cm^{-2}), and ϵ is the permittivity ($\text{CV}^{-1}\text{m}^{-1}$) at constant strain, (Ballantine et al., 1997). From the above relations it is obvious that the introduction of ozone causes electrical variation (represented in B) and are leading to changes in conductivity; this is something also confirmed from conductometric measurements. Furthermore ozone introduction results to mechanical variations by changing the elasticity of the sensing material and thus the stress (T). This variation leads to an increase in the wave velocity hence the frequency (see region marked as C) which is in a good agreement with other studies (Bhasker Raj et al., 2013) (Jakubik, 2011). Our results are described by equation 19. At region B as already said, the electrical variations stops and thus a constant electric field exists. Consequently, from equation 19; derives that the second term remains constant and the only term that varies is the stiffness (c^E) resulting in a relation between stress and strain (Young's modulus). Therefore, frequency changes are attributed to mechanical variations.

Repeatability

In conclusion, the repeatability of the photoreduction-oxidation process was tested and the results are shown below (fig. 32). As a test sample the filter of 30nm thickness was selected and its repeatability at the concentration of 500ppb for four consecutive cycles was examined, keeping constant all the other parameters that have been discussed earlier. It is obvious, that the sensor exhibits high repeatability, therefore high reliability.

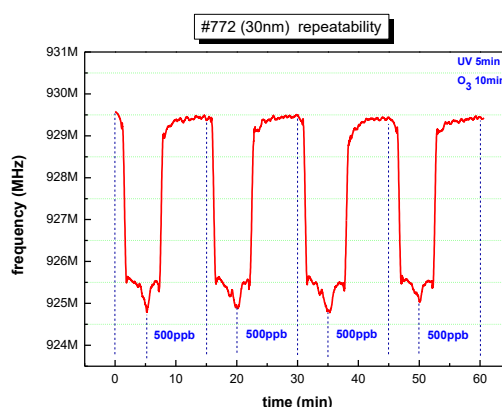


Figure 32: Repeatability of filter 930 MHz with 30nm thickness

It must be noted, that in the open literature, there is no similar work like the present and thus it was not possible to make a meaningful comparison with previous results. In a previous study, (Ippolito et al., 2005) InO_x has been used as selective layer onto $\text{ZnO}/\text{LiNbO}_3$ SAW device, and was tested for detection of reducing and also of oxidizing gases, with the lowest detected concentration found at 510ppb. Furthermore, the response was in the order of some kHz for operating frequencies of 139MHz approximately. The difference between this work with our results, is that they use layered SAW devices for increasing the sensitivity and operating temperatures ranging from 100 to 273°C. In comparison, we use only one layer on the top of the SAW device and all the experiments took place at RT conditions targeting in more cost effective and average real life applications. Still we manage to have a response of some MHz to every ozone level and especially to have a response at lower concentrations of 110ppb. In addition, in another study (Bhasker Raj et al., 2013) the research group has compared ZnO/SAW deposited by sputtering with other metal oxides (SnO_2 , TeO_2 and TiO_2) and found out that ZnO , in a parametric study of the thickness, shows higher responses under ammonia, which is a reducing gas. These results are in a good agreement with our work but still we achieved to have an adequate responses towards lower concentrations independently of film thickness. Also ZnO nanoparticles deposited by spin coating onto SAW devices were studied from another research group (Phan et al., 2012) for their application as hydrogen sensors and they resulted that a layered SAW structure has a frequency shift in low H_2 concentration at room temperature with good repeatability and stability. Again in this study the maximum measured shift was in the order of kHz. As opposed to our results, this good response was due to the post-annealing process and consequently to the crystallinity properties.

Conclusions

This work was based on the concept of investigating the ozone gas sensing properties of zinc oxide utilising conductometric measurements as bench-mark for surface acoustic wave gas sensors. The motivation was to compare high responses of metal oxide (ZnO) sensors utilising two different techniques, conductometric and SAW through a photoreduction and oxidation processes while studying experimentally additional phenomena beyond the already known due to the electric response i.e. relate to the mechanical properties of the applied sensing substrates (SAW). The novelty lied in the means of detecting low concentrations and the ability to distinguish between different ozone concentrations operating at room temperature.

In this context, the selected sensing material (ZnO) was deposited via a DC magnetron sputtering system depositing five different thicknesses (30nm, 63nm, 105nm, 205nm & 230nm) onto Corning glass substrates and also onto high frequency (\sim 1GHz) commercial SAW filters. The structural properties were studied by X-Ray diffraction patterns which reveals c-axis preferential orientation growth (002) plane, corresponding to $2\theta \approx 34^\circ$, and the intensities of the diffraction peaks were increased with increasing the thickness. Furthermore, cross sectional SEM was used to verify the thickness of the samples which were in good agreement with the a-step measurements. The optical characterization was carried out by spectrophotometry. The results from this measurements revealed good transparency for all thicknesses in the visible region, which accounted for more than 80% and the optical band gap was evaluated between 3.30-3.32eV for all samples.

The sensing properties were firstly studied as bench mark through a conductometric technique at a home-made apparatus at FORTH/IESL. The sensors responses varied from 3 to 5 orders of magnitude for every thickness, which is high enough for this deposition method. The repeatability results were very good in contrast to the stability which showed lower response compared to the initial measurement, carried out three months earlier.

The other method applied for the investigation of sensing properties utilised the surface acoustic waves concept. During this method, prior to the sensing measurements, the operational limitations of a SAW filter with a nominal frequency of 930MHz has been investigated. It was found that for thicknesses above 100nm the filters bandpass was destroyed due to the SAW intrinsic limited sensitivity to excess mass loading, and therefore couldn't be used as a sensor. Thus, only three samples with lower thicknesses (30nm, 63nm and 105nm) deposited on the filters have been studied.

Working with these samples, the mass loading effect was studied and a decrease of the centre frequency along with the increased film thickness has been observed, in line with the theoretical predictions. The acoustoelectric effect appeared to have the major impact on the results originating from changes in the films' conductivity states. The acoustoelectric effect revealed a good response of the sensor with the frequency shift of a few MHz, with the maximum value of 8-9 MHz for the first photoreduction- oxidation cycle. This effect also revealed that a two-step behaviour takes place during the oxidation process. The first step is attributed on the electrical variation and the second on the mechanical variations, originating from the piezoelectric properties of the substrate.

Comparisons between the two sensing techniques lead to the following remarks.

- Conductometric technique proved to be more efficient when used for film thicknesses above 100nm
- SAW technique proved to be more efficient when used for film thicknesses lower than 100nm
- Both techniques exhibited reversible photoreduction-oxidation processes
- Both exhibited good response
- Both are capable of detecting low ozone concentrations at RT conditions

Further research should focus on stability studies regarding SAW devices. Additionally, further investigation of the metal oxide sensing capabilities utilizing both techniques for the detection of reducing gasses is highly recommended. Finally,

future research should focus on the selectivity of the metal oxide sensors, to either different oxidizing or different reducing gasses.

References

- Ahn, M., Park, K., Heo, J., Park, J., Kim, D., Choi, K. J., ... Lee, J. (2013). Gas sensing properties of defect-controlled ZnO-nanowire gas sensor Gas sensing properties of defect-controlled ZnO-nanowire gas sensor, 263103(2008), 91–94.
<http://doi.org/10.1063/1.3046726>
- Arya, S. K., Saha, S., Ramirez-Vick, J. E., Gupta, V., Bhansali, S., & Singh, S. P. (2012). Recent advances in ZnO nanostructures and thin films for biosensor applications: Review. *Analytica Chimica Acta*, 737, 1–21.
<http://doi.org/10.1016/j.aca.2012.05.048>
- Atashbar, M. Z., Gong, B., Sun, H. T., Wlodarski, W., & Lamb, R. (1999). Investigation on ozone-sensitive In₂O₃ thin films. *Thin Solid Films*, 354(1), 222–226.
[http://doi.org/10.1016/S0040-6090\(99\)00405-8](http://doi.org/10.1016/S0040-6090(99)00405-8)
- Ayouchi, R., Leinen, D., Mart??n, F., Gabas, M., Dalchiele, E., & Ramos-Barrado, J. R. (2003). Preparation and characterization of transparent ZnO thin films obtained by spray pyrolysis. *Thin Solid Films*, 426(1–2), 68–77.
[http://doi.org/10.1016/S0040-6090\(02\)01331-7](http://doi.org/10.1016/S0040-6090(02)01331-7)
- Batzill, M., Chaka, a. M., & Diebold, U. (2004). Surface oxygen chemistry of a gas-sensing material: SnO₂ (101). *Europhysics Letters (EPL)*, 65(1), 61–67.
<http://doi.org/10.1209/epl/i2003-10044-0>
- Bedia, a., Bedia, F. Z., Aillerie, M., Maloufi, N., Ould Saad Hamady, S., Perroud, O., & Benyoucef, B. (2014). Optical, electrical and structural properties of nano-pyramidal ZnO films grown on glass substrate by spray pyrolysis technique. *Optical Materials*, 36(7), 1123–1130.
<http://doi.org/10.1016/j.optmat.2014.02.012>
- Bender, M., Fortunato, E., Nunes, P., Ferreira, I., Marques, A., Martins, R., ... Kiriakidis, G. (2003). Highly sensitive ZnO ozone detectors at room temperature. *Japanese Journal of Applied Physics, Part 2: Letters*, 42(4 B), 2–5.
<http://doi.org/10.1143/JJAP.42.L435>
- Bender, M., Gagaoudakis, E., Douloufakis, E., Natsakou, E., Katsarakis, N., Cimalla, V., ... Martins, R. (2002). Production and characterization of zinc oxide thin films for room temperature ozone sensing. *Thin Solid Films*, 418(1), 45–50.
[http://doi.org/10.1016/S0040-6090\(02\)00588-6](http://doi.org/10.1016/S0040-6090(02)00588-6)
- Bhasker Raj, V., Singh, H., Nimal, A. T., Tomar, M., Sharma, M. U., & Gupta, V. (2013). Effect of metal oxide sensing layers on the distinct detection of ammonia using surface acoustic wave (SAW) sensors. *Sensors and Actuators, B: Chemical*, 187, 563–573. <http://doi.org/10.1016/j.snb.2013.04.063>
- Bochenkov, V. E., & Sergeev, G. B. (2010). Sensitivity , Selectivity , and Stability of Gas-Sensitive Metal-Oxide Nanostructures, 3, 31–52.
- Cheeke, J. D. N., & Wang, Z. (1999). Acoustic wave gas sensors. *Sensors and*

Actuators B: Chemical, 59(2–3), 146–153. [http://doi.org/10.1016/S0925-4005\(99\)00212-9](http://doi.org/10.1016/S0925-4005(99)00212-9)

Cheng, X. L., Zhao, H., Huo, L. H., Gao, S., & Zhao, J. G. (2004). ZnO nanoparticulate thin film: Preparation, characterization and gas-sensing property. *Sensors and Actuators, B: Chemical*, 102(2), 248–252.
<http://doi.org/10.1016/j.snb.2004.04.080>

Chien, F. S., Wang, C., Chan, Y., Lin, H., Chen, M., & Wu, R. (2010). Sensors and Actuators B : Chemical Fast-response ozone sensor with ZnO nanorods grown by chemical vapor deposition, 144, 120–125.
<http://doi.org/10.1016/j.snb.2009.10.043>

Christoulakis, S., Suchea, M., Koudoumas, E., Katharakis, M., Katsarakis, N., & Kiriakidis, G. (2006). Thickness influence on surface morphology and ozone sensing properties of nanostructured ZnO transparent thin films grown by PLD. *Applied Surface Science*, 252(15), 5351–5354.
<http://doi.org/10.1016/j.apsusc.2005.12.071>

Comini, E., Faglia, G., & Sberveglieri, G. (2009). *Solid State Gas Sensing. Journal of Chemical Information and Modeling* (Vol. 53).
<http://doi.org/10.1017/CBO9781107415324.004>

de Lacy Costello, B. P. J., Ewen, R. J., Ratcliffe, N. M., & Richards, M. (2008). Highly sensitive room temperature sensors based on the UV-LED activation of zinc oxide nanoparticles. *Sensors and Actuators, B: Chemical*, 134(2), 945–952.
<http://doi.org/10.1016/j.snb.2008.06.055>

Eranna, G., Joshi, B. C., Runthala, D. P., Gupta, R. P., Eranna, G., Joshi, B. C., ... Gupta, R. P. (2016). Oxide Materials for Development of Integrated Gas Sensors — A Comprehensive Review Oxide Materials for Development of Integrated Gas Sensors — A Comprehensive Review, 8436(September).
<http://doi.org/10.1080/10408430490888977>

Gagaoudakis, E., Bender, M., Douloufakis, E., Katsarakis, N., Natsakou, E., Cimalla, V., & Kiriakidis, G. (2001). The influence of deposition parameters on room temperature ozone sensing properties of InO_x® lms. *Sensors And Actuators, 80*, 155–161. [http://doi.org/10.1016/S0925-4005\(01\)00908-X](http://doi.org/10.1016/S0925-4005(01)00908-X)

Garza, H. P. (2013). *Graphene-Propagating wave interaction by means of surface acoustic wave devices*.

Hatch, S. (2000). Surface Acoustic Waves on Piezoelectric Media, (October).

Hoummady, M., Campitelli, A., & Włodarski, W. (1999). Acoustic wave sensors: design, sensing mechanisms and applications. *Smart Materials and Structures*, 6(6), 647–657. <http://doi.org/10.1088/0964-1726/6/6/001>

Huang, J., Wu, Y., Gu, C., Zhai, M., Sun, Y., & Liu, J. (2011). Fabrication and gas-sensing properties of hierarchically porous ZnO architectures. *Sensors and Actuators, B: Chemical*, 155(1), 126–133.
<http://doi.org/10.1016/j.snb.2010.11.036>

- Ippolito, S. J., Kandasamy, S., Kalantar-Zadeh, K., Wlodarski, W., Galatsis, K., Kiriakidis, G., ... Suchea, M. (2005). Highly sensitive layered ZnO/LiNbO₃ SAW device with InO x selective layer for NO₂ and H₂ gas sensing. *Sensors and Actuators, B: Chemical*, 111–112(SUPPL.), 207–212.
<http://doi.org/10.1016/j.snb.2005.07.046>
- Jakubik, W. P. (2011). Surface acoustic wave-based gas sensors. *Thin Solid Films*, 520(3), 986–993. <http://doi.org/10.1016/j.tsf.2011.04.174>
- Jiménez-Cadena, G., Riu, J., & Rius, F. X. (2007). Gas sensors based on nanostructured materials. *The Analyst*, 132, 1083–1099.
<http://doi.org/10.1039/b704562j>
- Jin, M., & Ying, L. S. (1994). Letter Preparation of ZnO films by reactive evaporation, 237, 16–18.
- Kenanakis, G., Vernardou, D., Koudoumas, E., Kiriakidis, G., & Katsarakis, N. (2007). Ozone sensing properties of ZnO nanostructures grown by the aqueous chemical growth technique. *Sensors and Actuators, B: Chemical*, 124(1), 187–191. <http://doi.org/10.1016/j.snb.2006.12.033>
- Kim, W., Choi, M., & Yong, K. (2015). Sensors and Actuators B : Chemical Generation of oxygen vacancies in ZnO nanorods / films and their effects on gas sensing properties. *Sensors & Actuators: B. Chemical*, 209, 989–996.
<http://doi.org/10.1016/j.snb.2014.12.072>
- Kiriakidis, G., Moschovis, K., Kortidis, I., & Binas, V. (2012). Ultra-low gas sensing utilizing metal oxide thin films. *Vacuum*, 86(5), 495–506.
<http://doi.org/10.1016/j.vacuum.2011.10.013>
- Kirschbrown, J. (2007). RF/DC Magnetron Sputtering. *Unc.Edu*, 1, 1–4. Retrieved from http://www.unc.edu/~justink/RFDC_Sputtering.pdf
- Kirschner, J. (2010). Surface Acoustic Wave Sensors (SAWS): Design for Application. *Microelectromechanical Systems*, 1–11.
- Kortidis, I., Moschovis, K., Mahmoud, F. A., & Kiriakidis, G. (2009). Structural analysis of aerosol spray pyrolysis ZnO films exhibiting ultra low ozone detection limits at room temperature. *Thin Solid Films*, 518(4), 1208–1213.
<http://doi.org/10.1016/j.tsf.2009.08.018>
- Lee, G. H., Kawazoe, T., & Ohtsu, M. (2002). Difference in optical bandgap between zinc-blende and wurtzite ZnO structure formed on sapphire (0001) substrate. *Solid State Communications*, 124(5–6), 163–165. [http://doi.org/10.1016/S0038-1098\(02\)00537-9](http://doi.org/10.1016/S0038-1098(02)00537-9)
- Li, Z., & Gao, W. (2004). ZnO thin films with DC and RF reactive sputtering. *Materials Letters*, 58(7–8), 1363–1370. <http://doi.org/10.1016/j.matlet.2003.09.028>
- Lin, S., Huang, J., & Lii, D. (2005). Effect of substrate temperature on the properties of Ti-doped ZnO films by simultaneous rf and dc magnetron sputtering, 90, 22–30. <http://doi.org/10.1016/j.matchemphys.2004.08.040>
- Look, D. C. (2001). Recent advances in ZnO materials and devices. *Materials Science*

- and Engineering B: Solid-State Materials for Advanced Technology*, 80(1–3), 383–387. [http://doi.org/10.1016/S0921-5107\(00\)00604-8](http://doi.org/10.1016/S0921-5107(00)00604-8)
- Ma, J., Ji, F., Ma, H., & Li, S. (1996). Electrical and optical properties of ZnO : A1 films prepared by an evaporation method. *Thin Solid Films*, 279, 213–215. [http://doi.org/10.1016/0040-6090\(95\)08173-9](http://doi.org/10.1016/0040-6090(95)08173-9)
- Magnetics, M. (n.d.). Magnetron Sputtering Technology. Retrieved from http://www.directvacuum.com/pdf/what_is_sputtering.pdf
- Manohar, G. (2012). Investigation of Various Surface Acoustic Wave Design Configurations for Improved Sensitivity, (January). Retrieved from <http://scholarcommons.usf.edu/etd/4365/>
- Mart??nez-P??rez, L., Mu??oz-Aguirre, N., Mu??oz-Aguirre, S., & Zelaya-Angel, O. (2015). Nanometric structures of highly oriented zinc blende ZnO thin films. *Materials Letters*, 139, 63–65. <http://doi.org/10.1016/j.matlet.2014.10.054>
- Martins, R., Fortunato, E., Nunes, P., Ferreira, I., Marques, A., Bender, M., ... Kiriakidis, G. (2004). Zinc oxide as an ozone sensor. *Journal of Applied Physics*, 96(3), 1398–1408. <http://doi.org/10.1063/1.1765864>
- Matatagui, D., Fernandez, M. J., Fontecha, J. L., Santos, J. P., Gràcia, I., Cané, C., & Horrillo, M. C. (2015). Sensors and Actuators B : Chemical Propagation of acoustic waves in metal oxide nanoparticle layers with catalytic metals for selective gas detection. *Sensors & Actuators: B. Chemical*, 217, 65–71. <http://doi.org/10.1016/j.snb.2014.12.076>
- Musat, V., Rego, A. M., Monteiro, R., & Fortunato, E. (2008). Microstructure and gas-sensing properties of sol-gel ZnO thin films. *Thin Solid Films*, 516(7), 1512–1515. <http://doi.org/10.1016/j.tsf.2007.07.198>
- Nakamura, N., Cochran, S., Hubschen, G., Uchino, K., Kurosawa, M. K., Yamashita, Y., ... Courtney. (2012). *Ultrasonic transducers*. (K. Nakamura, Ed.). Woodhead.
- Özgür, Ü., Alivov, Y. I., Liu, C., Teke, A., Reshchikov, M. A., Doğan, S., ... Morkoç, H. (2005). A comprehensive review of ZnO materials and devices. *Journal of Applied Physics*, 98(4), 1–103. <http://doi.org/10.1063/1.1992666>
- Özgür, Ü., Hofstetter, D., & Morkoç, H. (2010). ZnO Devices and Applications: A Review of Current Status and Future Prospects. *Proceedings of the IEEE*, 98(7), 1255–1268. <http://doi.org/10.1109/JPROC.2010.2044550>
- Ozone and Health. (2015). Retrieved from www.arb.ca.gov
- Shokry Hassan, H., Kashyout, A. B., Morsi, I., Nasser, A. A. A., & Ali, I. (2014). Synthesis, characterization and fabrication of gas sensor devices using ZnO and ZnO:In nanomaterials. *Beni-Suef University Journal of Basic and Applied Sciences*, 3(3), 216–221. <http://doi.org/10.1016/j.bjbas.2014.10.007>
- Sucea, M., Christoulakis, S., Moschovis, K., Katsarakis, N., & Kiriakidis, G. (2006). ZnO transparent thin films for gas sensor applications. *Thin Solid Films*, 515(2 SPEC. ISS.), 551–554. <http://doi.org/10.1016/j.tsf.2005.12.295>

- Tseng, J.-Y., Chen, Y.-T., Lin, C. J., Liu, W.-J., Wang, C. C., Chen, Q. R., ... Chou, T. B. (2015). The optical, electrical, and nanomechanical properties of ZnO thin films. *Optik - International Journal for Light and Electron Optics*, 126(21), 3263–3266. <http://doi.org/10.1016/j.ijleo.2015.07.126>
- Wasa, K., & Hayakawa, S. (2012). *Handbook of Sputter Deposition Technology Fundamentals and Applications for Functional Thin Films, Nanomaterials, and MEMS*. <http://doi.org/10.1016/B978-1-4377-3483-6.00006-1>
- Wei, A., Pan, L., & Huang, W. (2011). Recent progress in the ZnO nanostructure-based sensors. *Materials Science and Engineering B: Solid-State Materials for Advanced Technology*, 176(18), 1409–1421. <http://doi.org/10.1016/j.mseb.2011.09.005>
- Morgan D., (2007) Surface Acoustic wave filters: with applications to electronic communications and signal processing [second edition]. Retrieved from <http://store.elsevier.com/Surface-Acoustic-Wave-Filters/David-Morgan/isbn-9780080550138/>
- Ballantine D. S., Martin S. J., Ricco A. J., Frye G. C, Wohltjen H., White R. M. and Zellers E.T. (1996) Acoustic Wave Sensors: Theory, Design, and Physico-Chemical Applications. Retrieved from <http://www.hbuk.co.uk/ap/>
- Binas V., Kortidis I., Gagaooudakis E., Moschovis K. and Kiriakidis G. (2016). Ageing Resistant Indium Oxide Ozone Sensing Films. *Sensor Letters*, Volume 14, Number 6, June 2016, pp. 563-566(4) <http://www.ingentaconnect.com/content/asp/senlet/2016/00000014/00000006/art00001>

Appendix I

Tel: +44 1460 256 100
Fax: +44 1460 256 101
www.golledge.com

Golledge

Golledge Electronics Ltd
Eaglewood Park, Ilminster
Somerset, TA19 9DQ, UK

RF SAW Filter 930.5 MHz
Part No: MA05185

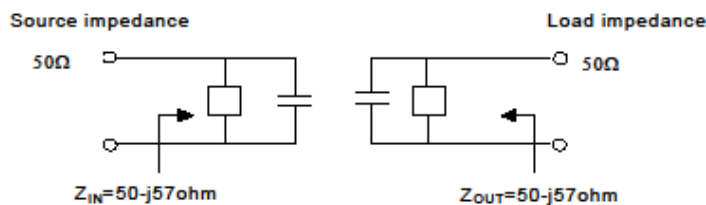
Model: TA930H1
REV NO.: 4

A. MAXIMUM RATING:

1. Input Power Level: 10dBm
2. DC Voltage : 3V
3. Operating Temperature: -10°C to +50°C
4. Storage Temperature: -40°C to +85°C

B. ELECTRICAL CHARACTERISTICS:

| Item | Unit | Min. | Type. | Max. | Note |
|---|------|-----------|-------|------|------|
| Center Frequency Fc | MHz | - | 930.5 | - | - |
| Insertion Loss (928.5 ~ 932.5 MHz) IL | dB | - | 3.2 | 4.5 | - |
| Amplitude Ripple (928.5 ~ 932.5 MHz) | dB | - | 0.5 | 2 | - |
| Relative Attenuation (relative to 0 dB) | | | | | |
| 400 ~ 880 MHz | dB | 35 | 50 | - | - |
| 884.8 ~ 890.2 MHz | dB | 45 | 50 | - | - |
| 906.8 ~ 911.2 MHz | dB | 30 | 41 | - | - |
| 980 ~ 1300 MHz | dB | 35 | 60 | - | - |
| Impedance at Fc ; Input Impedance | | 50-j57ohm | | | |
| Output Impedance | | 50-j57ohm | | | |



Tel: +44 1460 256 100
Fax: +44 1460 256 101
www.golledge.com

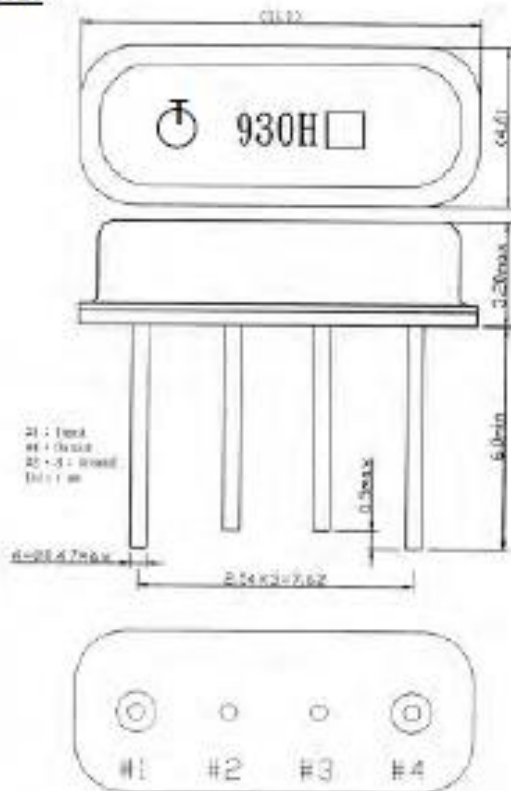
Golledge

Golledge Electronics Ltd
Eaglewood Park, Ilminster
Somerset, TA19 9DQ, UK

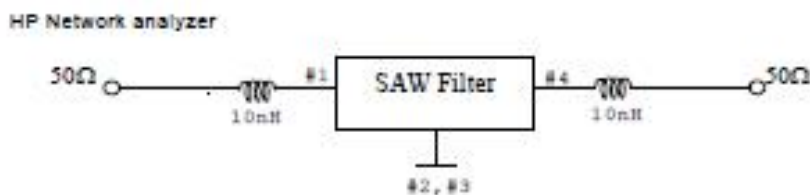
RF SAW Filter 930.5 MHz
Part No: MA05185

Model: TA930H1
REV NO.: 4

C. OUTLINE DRAWING:



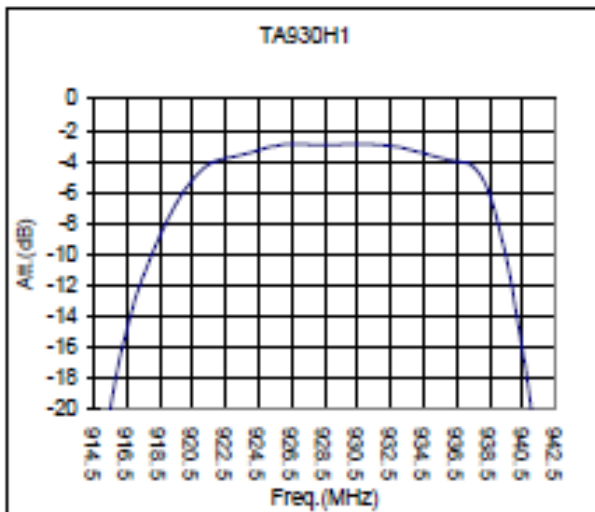
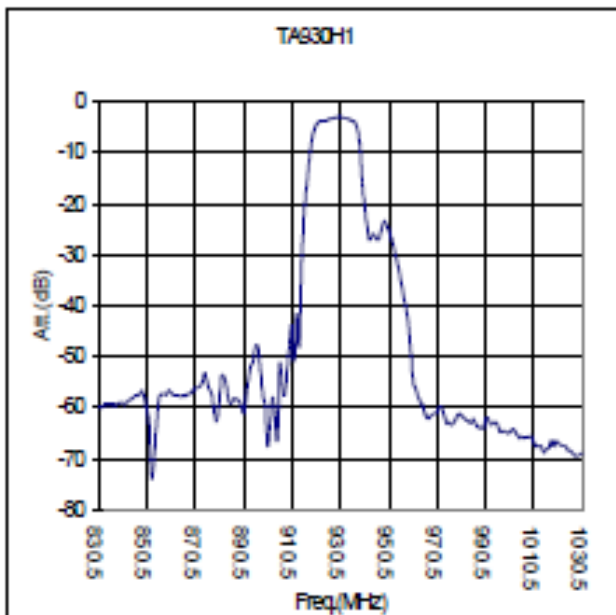
D. MEASUREMENT CIRCUIT:



RF SAW Filter 930.5 MHz
Part No: MA05185

Model: TA930H1
REV NO.: 4

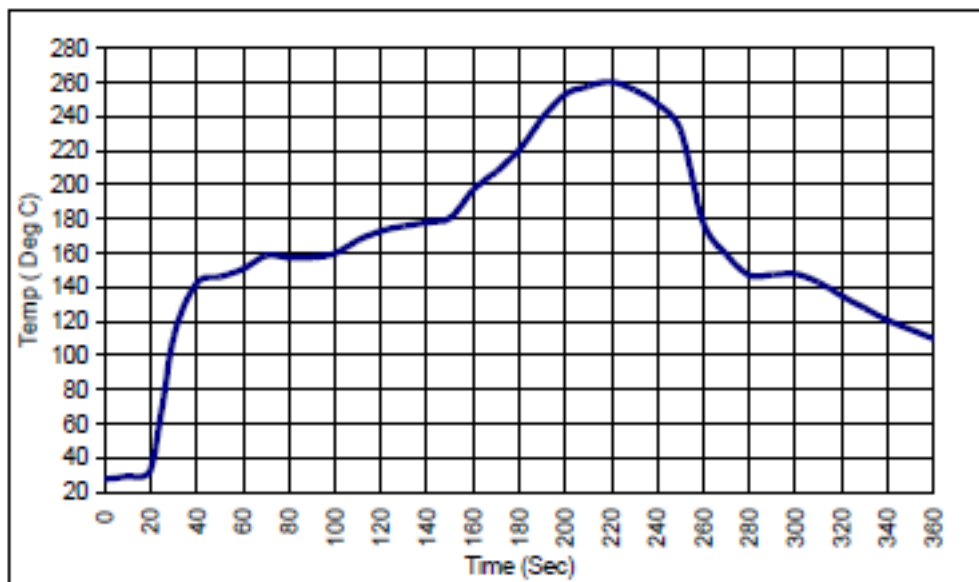
E. FREQUENCY CHARACTERISTICS:



RF SAW Filter 930.5 MHz
Part No: MA05185

Model: TA930H1
REV NO.: 4

F. RECOMMENDED REFLOW PROFILE :



Appendix II

